

# *Spitzer* Mapping of PAH and H<sub>2</sub> features in Photodissociation Regions

B. Fleming

Department of Physics and Astronomy, Johns Hopkins University, Baltimore, MD 21218

flembri@pha.jhu.edu

K. France

Center for Astrophysics and Space Astronomy, University of Colorado, Boulder, CO 80309

R. E. Lupu

Department of Physics and Astronomy, University of Pennsylvania, Philadelphia, PA 19104

and

S. R. McCandliss

Department of Physics and Astronomy, Johns Hopkins University, Baltimore, MD 21218

Received \_\_\_\_\_; accepted \_\_\_\_\_

## ABSTRACT

The mid-infrared (MIR) spectra of dense photodissociation regions (PDRs) are typically dominated by emission from polycyclic aromatic hydrocarbons (PAHs) and the lowest pure rotational states of molecular hydrogen ( $\text{H}_2$ ); two species which are probes of the physical properties of gas and dust in intense UV radiation fields. We utilize the high angular resolution of the Infrared Spectrograph on the *Spitzer Space Telescope* to construct spectral maps of the PAH and  $\text{H}_2$  features for three of the best studied PDRs in the galaxy, NGC 7023, NGC 2023 and IC 63. We present spatially resolved maps of the physical properties, including the  $\text{H}_2$  ortho-to-para ratio, temperature, and  $G_o/n_H$ . We also present evidence for PAH dehydrogenation, which may support theories of  $\text{H}_2$  formation on PAH surfaces, and a detection of preferential self-shielding of ortho- $\text{H}_2$ . All PDRs studied exhibit average temperatures of  $\sim 500 - 800$  K, warm  $\text{H}_2$  column densities of  $\sim 10^{20} \text{ cm}^{-2}$ ,  $G_o/n_H \sim 0.1 - 0.8$ , and ortho-to-para ratios of  $\sim 1.8$ . We find that while the average of each of these properties is consistent with previous single value measurements of these PDRs, when available, the addition of spatial resolution yields a diversity of values with gas temperatures as high as 1500 K, column densities spanning  $\sim 2$  orders of magnitude, and extreme ortho-to-para ratios ( $R_{OP}$ ) of  $R_{OP} < 1$  and  $R_{OP} > 3$ .

*Subject headings:* ISM:clouds — ISM: lines and bands — ISM: photon-dominated region — ISM: individual (NGC 7023, NGC 2023, IC 63) — ISM: molecules — infrared: ISM

## 1. Introduction

Photodissociation regions (PDRs) around hot stars are the boundaries between the ionized HII region and the surrounding molecular clouds. PDRs consist of layers of atomic and molecular emission with a chemical profile dictated by the ratio  $G_o/n_H$ , where  $G_o$  is the strength of the local UV radiation field (912 – 2000 Å) in units of the Habing flux ( $1.6 \times 10^{-3}$  erg cm<sup>-2</sup> s<sup>-1</sup>, Habing (1968)) and  $n_H$  is the local hydrogen density (Hollenbach & Tielens 1997). The typical mid-infrared (MIR; 5-35 μm) spectrum of a PDR is dominated by the stretching and bending modes of polycyclic aromatic hydrocarbons (PAHs) excited by the absorption of individual UV photons and by the lowest pure rotational lines of molecular hydrogen (Leger & Puget 1984). H<sub>2</sub> is formed on the surface of dust grains and is destroyed by photodissociation within PDRs. Its formation rate has been found to be related to PAH abundance (Habart et al. 2004), suggesting that there may be an observational relationship between these two species. Both PAHs and H<sub>2</sub> have been shown to be valuable probes of the physical conditions within PDRs (Bakes & Tielens 1994; Draine & Bertoldi 1996; Hollenbach & Tielens 1997; Berné et al. 2009).

PAH emission in the MIR is dominated by the five broad emission features centered at 6.2 μm, 7.7 μm, 8.6 μm, 11.3 μm and 12.7 μm. These, along with features at 3.3 μm and 17 μm, are also referred to as the Unidentified Infrared (UIR) features and the Aromatic Infrared Bands (AIBs). Studies have suggested that each of the major PAH bands is actually a blend of emission from PAHs of various sizes, surface structures, and charges, therefore the relative shapes, centroids and flux ratios with respect to the other bands vary depending on the physical properties of the observed PAHs (Bakes & Tielens 1994; Peeters et al. 2002; van Dienenhoven et al. 2004). Laboratory measurements have shown that the features attributed to carbon-hydrogen (C-H) bond bending, namely the 3.3 μm, 11.3 μm and 12.7 μm bands, are dominant for a population of neutral PAHs, however the

carbon-carbon (C-C) stretching modes, from 6 - 9  $\mu\text{m}$ , are the dominant emission from PAH cations ( $\text{PAH}^+$ ) (Allamandola et al. 1999; Hudgins & Allamandola 1999). In recent years the ratio of C-C emission to C-H emission, most notably the 6.2  $\mu\text{m}$  or 7.7  $\mu\text{m}$  to 11.3  $\mu\text{m}$  bands, has become a method of estimating the charge state of a PAH cloud (Joblin et al. 1996; Galliano et al. 2008). A smaller number of studies have shown that the ratio of the 12.7  $\mu\text{m}$  emission, which arises from duo and trio C-H out-of-plane bending modes, to the 11.3  $\mu\text{m}$  singlet C-H out-of-plane bending mode is a probe of the PAH surface structure (Duley & Williams 1981; Hony et al. 2001; Tielens 2008). For smaller PAHs (with fewer than 50 carbon atoms),  $I_{12.7}/I_{11.3}$  may be an indicator of dehydrogenation, or the breakdown of duo and trio C-H bonds into solo bonds.

In this paper, we present spectral line maps of the  $\text{H}_2$  and PAH emission measured by the *Spitzer Space Telescope* from four of the best studied PDRs; NGC 7023, IC 63 and two separate regions in NGC 2023 (Figures 1, 2, 3). All three PDRs are known to exhibit UV fluorescence of  $\text{H}_2$  (France et al. (2009) and references therein). We utilize the high angular resolution of the Infrared Spectrograph (IRS; Houck et al. (2004)) onboard *Spitzer* to investigate the spatial variation of the temperature, column density, and ortho-to-para ratio of the lowest pure rotational states of  $\text{H}_2$ , the ratio  $G_o/n_H$  determined from the ionization state of the PAHs, and we address the possibility of dehydrogenation of PAHs across the observed regions. We present these maps and the methods used to generate them in §3. In §4 we present a summary of the new information revealed by the mapping technique for each PDR, and address the agreement between our measurements and previous observations. In §5 we address and similarities or differences between the PDRs and summarize our findings. A summary of the basic properties of the regions is presented in Table 1.

## 2. Observations and Data Reduction

### 2.1. Data Cube Assembly

*Spitzer* data products were downloaded from the *Spitzer* Science Center (SSC) archive for NGC 7023, IC 63, and two locations in NGC 2023: NGC 2023 North (NGC 2023N), located  $\sim 160''$  north of the central star HD 37903, and NGC 2023 South (NGC 2023S), located  $\sim 78''$  south of HD 37903. *IRS* short wavelength low resolution (R  $\sim 60 - 127$ , SL) 5 - 14  $\mu\text{m}$  Basic Calibrated Data (BCD) spectra were obtained for each nebula. For a portion of NGC 7023 and for all of NGC 2023N we also obtained long wavelength low resolution (R  $\sim 57 - 126$ , LL) 14 - 38  $\mu\text{m}$  spectra. These spectra were assembled into data cubes using the CUBISM software (Smith et al. 2007)

*Spitzer* BCD products require background and bad pixel subtraction. In IC 63, the outrigger exposures (the exposures of channel not centered on the target) were clear of nebulosity and therefore supplied a suitable background exposure. This was not the case for the extended PDRs NGC 7023 and NGC 2023. For NGC 2023S a dedicated sky exposure was taken and included in the BCD data package. To account for background emission in NGC 7023 and NGC 2023N, we searched the SSC archive for point source spectra of objects within  $10^\circ$  of declination of each of our targets taken within  $\pm 3$  days of our data. If the outrigger orders of these exposures were free of stars or nebulosity, then it was considered suitable for background subtraction.

Bad pixels were removed using the CUBISM automated bad pixel routine as well as by interactive selection. Mapping observations with overlapping slits along the slit axis required editing of the default 'WAVSAMP' to eliminate contamination caused by the higher noise at the slit endpoints. The resulting 3-D data cubes (two spatial dimensions and one spectral,  $N \times M \times \lambda$ ) from each of the two IRS channels were merged into one by

averaging the regions of overlap between each of the spectral orders (the bonus orders were ignored). The spatial dimensions of the data cubes are  $\sim 1.8 \times 1.8''/\text{pixel}$ . A summary of the *Spitzer* AORs, program ID's and background program IDs for each of our datasets is listed in Table 2.

## 2.2. Spectral Feature Fitting

Each 1-D spectrum in the data cube was fit using the PAHFIT IDL routine (Smith et al. 2007). PAHFIT uses Drude profiles to fit the broad PAH features and Gaussians to fit the atomic and molecular lines, including the  $\text{H}_2$  0-0 S(0) – S(7) rotational lines. The use of Drude profiles for the aromatic bands has been shown to recover  $\sim 2$ -6 times more flux in the broad wings of the  $7.7 \mu\text{m}$  and  $8.6 \mu\text{m}$  features than spline fitting or Gaussian profiles (Smith et al. 2006). The resulting integrated fluxes for each feature were then reassembled into maps.

PAHFIT has a built-in routine to correct for extinction, including the silicate absorption features at 10 and  $18 \mu\text{m}$ . To improve the spatial correlation of the extinction fitting, we re-binned our spectral maps into larger,  $18 \times 18''$  pixels ( $\sim 5 \times 5$  IRS pixels). The resulting extinction values were extrapolated, smoothed and then applied to the original maps using the PAHFIT extinction curve. For the majority of our sample the MIR extinction is nearly negligible (the optical depth at  $9.7 \mu\text{m}$ ,  $\tau_{9.7} < 0.2$ ), which is consistent with the *ISO* derived global value inferred from observation of HD 200775 for NGC 7023 (Fuente et al. 2000), and also with extrapolations of optical and near-IR measured extinctions into the MIR (Draine & Bertoldi 2000).

The data for NGC 2023N has an anomalous absorption feature between  $9.3$  and  $10.7 \mu\text{m}$  with a position dependent centroid. The average full width at half maximum of the

feature is  $\sim 0.32 \mu\text{m}$  and the average integrated flux is  $\sim 27.25 \text{ MJy } \mu\text{m sr}^{-1}$ . The centroid varies between  $\sim 9.25 \mu\text{m}$  and  $10.65 \mu\text{m}$ . We attempt to correct for by first determining the centroid and then scaling the original spectra over that region using a multi-gaussian fit and the average FWHM and integrated flux listed above. This correction introduces a systematic uncertainty to the  $\text{H}_2$  S(3) rotational line. Due to the importance of S(3) as the primary SL band ortho-rotational line detected in NGC 2023N, we utilize S(3) in our analysis despite the uncertainty. We estimate the error in the S(3) flux to vary from  $\sim 0\%$  near the edges of the observed region to up to  $40\%$  in the middle, however we see no position dependant artifacts in our temperature, column density, or  $\text{H}_2$  ortho-to-para ratio maps (§3). Nevertheless, this ad hoc correction should be taken into account when considering the validity of our results for that PDR.

### 3. Spectral Maps

Spectral maps of the total  $\text{H}_2$  and PAH emission and the resulting line ratios and diagnostics presented in this section are included in Figures 4 – 7. Figures 4 – 7 (a) and (b) represent the total detected SL band PAH and  $\text{H}_2$  emission respectively. Figures 4 – 7 (c) and (d) represent the ratio of the  $7.7 \mu\text{m}$  to  $11.3 \mu\text{m}$  and  $12.7 \mu\text{m}$  to  $11.3 \mu\text{m}$  PAH bands respectively. Figures 4 – 7 (e), (f), and (g) represent the calculated  $\text{H}_2$  column densities, temperatures, and ortho-to-para ratios. Figures 4 – 7 (h) show the calculated values of  $G_o/n_H$ . In the following section we outline how each of these maps is constructed and discuss their physical interpretation.<sup>1</sup>

For consistency, spectral analysis is only performed on data from the IRS SL channel,

---

<sup>1</sup>Maps of each individual  $\text{H}_2$  rotation line, the major PAH features, and properties calculated in this paper are available online at [www.pha.jhu.edu/~flem bri/PDRs](http://www.pha.jhu.edu/~flem bri/PDRs).

except where noted. Therefore when we refer to PAH emission, we are neglecting the PAH features around  $17 \mu\text{m}$ , and when we refer to  $\text{H}_2$  emission, we are neglecting S(0) and S(1). All maps have been oriented so that north is up. A summary of the average values for each of the properties calculated is presented in Table 3. These average values are not the same as the values obtained if the entire observed region was rebinned into a single pixel, however, as equal weight is given to each pixel regardless of the flux of the lines used to calculate that property. Therefore, the temperature of a pixel with an order of magnitude lower  $\text{H}_2$  flux than another is counted the same when computing the average, even though the pixel with the higher flux would dominate in a larger aperture. Single value measurements are already available for these PDRs and listed in Table 1.

### 3.1. PAH and $\text{H}_2$ Emission

Individual spectral maps were constructed for the major *Spitzer* SL band PAH features ( $6.2, 7.7, 8.6, 11.3,$  and  $12.7 \mu\text{m}$ ) and  $\text{H}_2$  0–0 S( $J = 2 - 7$ ) rotational emission lines using the extinction corrected line fluxes output by the PAHFIT routine. The signal-to-noise of the integrated line flux extracted from each 1-D spectra was required to be  $\geq 3$  for the line to be included in its spectral map. Figures 4 – 7 (a) and (b) represent the sum of the individual PAH and  $\text{H}_2$  maps respectively and therefore are maps of the total *detected* PAH and  $\text{H}_2$  flux in the  $5 - 14 \mu\text{m}$  bandpass.

The individual PAH features are strong, especially in NGC 7023 and NGC 2023, and Figures 4 – 7 (a) represent the sum of the individual spectral maps with nearly complete coverage of the observed PDR in all bands. Figures 4 – 7 (b), however, only represent a lower limit on the total SL band  $\text{H}_2$  emission as the signal-to-noise of the higher  $J$  lines is often below our  $S/N \geq 3$  threshold. Throughout this paper we neglect the  $\text{H}_2$  S(6) ( $6.11 \mu\text{m}$ ) line as it is heavily blended with the stronger  $6.2 \mu\text{m}$  PAH feature and therefore cannot



be reliably extracted.

### 3.2. PAH Band Ratios

In recent years measurements of the PAH ionization state have become important diagnostic tools for PDRs. Berné et al. (2007) successfully isolated PAH<sup>0</sup> and PAH<sup>+</sup> emission using blind signal separation techniques, showing that PAH<sup>+</sup> emission is most prevalent closer to the HII region where the radiation field is stronger. We investigate the degree of PAH ionization using the ratio of the 7.7  $\mu\text{m}$  C-C stretching modes to the 11.3  $\mu\text{m}$  C-H out-of-plane bending mode. Laboratory studies have shown that ionized PAHs emit more in the C-C modes relative to the C-H bending modes than neutral PAHs, therefore Figures 4 – 7 (c) are representations of the ionization state of the PAH molecules in the PDRs (Joblin et al. 1996; Allamandola et al. 1999). The ratio  $I_{7.7}/I_{11.3}$  is expected to be  $\sim 1.3$  for a fully neutral column of PAHs and  $\sim 12$  for a completely ionized column (Li & Draine 2001).

The maps presented in Figures 4 – 7 (d) represent the surface structure of the PAHs given by the ratio  $I_{12.7}/I_{11.3}$ . PAHs can be stripped down to their carbon cores, or even dissociated via carbon fragment loss, by absorbing UV photons with energies as low as 5 – 8 eV (Le Page et al. 2003). The dehydrogenation of a PAH decreases emission in the C-H singlet bands (centered at 11.3  $\mu\text{m}$ ) relative to the duo and triplet bands (centered at 12.7  $\mu\text{m}$ ), however this relation is not fully understood, therefore we will focus only on what the trends in  $I_{12.7}/I_{11.3}$  reveal rather than the absolute values of the ratios.

### 3.3. H<sub>2</sub> Temperature, Column Density, and Ortho-to-Para Ratio

We can determine a gas temperature,  $T_{gas}$ , using the pure rotational states of H<sub>2</sub>. These transitions have small critical densities and therefore can be assumed to be dominated by collisional de-excitation (see chap. 9.7.3 of Tielens (2005) for a review). Assuming thermodynamic equilibrium and a Maxwell-Boltzmann distribution,

$$\ln\left(\frac{N_{J+2}}{g_{J+2}}\right) = \ln(N_{H_2}) - \frac{E_{J+2}}{kT_{gas}}, \quad (1)$$

where  $E_{J+2}$  is the energy and  $g_{J+2}$  is the statistical weight of the  $J+2$  state. H<sub>2</sub> is a homonuclear molecule and hence has no dipole allowed pure rotational transitions, therefore we only detect quadrupole transitions with  $\Delta J = 2$ . The statistical weight of the  $J$  state is,

$$\begin{aligned} g_{J=0,2,4,6\dots} &= 2J + 1 \\ g_{J=1,3,5,7\dots} &= (2J + 1)R_{OP} \end{aligned}, \quad (2)$$

where  $R_{OP}$  is the ortho-to-para ratio of the H<sub>2</sub>, which is 3 in a gas at temperature greater than  $\sim 250$  K in local thermal equilibrium (LTE) (Sternberg & Neufeld 1999). For H<sub>2</sub> out of LTE, the ortho-rotational lines (odd  $J$  states corresponding to parallel nuclear spins) will be offset from the para-rotational lines (even  $J$  states with anti-parallel spins), resulting in a “zig-zag” distribution. The column density,  $N_{J+2}$ , of the  $J+2$  state is determined by the Einstein  $A_{S(J)}$  coefficient,

$$N_{J+2} = \frac{4\pi f_{S(J)}}{A_{S(J)}hc/\lambda_{S(J)}}, \quad (3)$$

where  $S(J)$  denotes the H<sub>2</sub>  $0-0$  ( $J+2$ )  $\rightarrow$   $J$  rotational transition and  $f_{S(J)}$  is the measured flux density of the rotational emission line. This equation is valid only because the H<sub>2</sub> lines are dipole-forbidden and therefore optically thin.

In a uniform, single temperature gas with  $R_{OP} = 3$ , the curve established by Equation [1] will be a straight line on a log-linear plot. The slope of this line is defined by the  $H_2$  rotational temperature. In a single temperature gas, the temperature, column density, and  $R_{OP}$  can be determined by iterating  $R_{OP}$  until the data can be fit by a single  $N_{H_2}$  and  $T_{gas}$ .

PDRs consist of a multiphase gas that can be approximated by a low density, diffuse medium interspersed with high density clumps or filaments (Chokshi et al. 1988; Sellgren et al. 1992). The majority of the  $H_2$  is in the cool, low density phase, however the emission spectrum in the SL band is dominated by the higher density warm component, often making up  $< 1\%$  of the total  $H_2$  column (Figure 8). For the purposes of this study, we assume a single temperature dominates the  $H_2$  S(2) – S(5) rotational emission lines and fit a temperature,  $N_{H_2}$  and  $R_{OP}$  accordingly. To construct maps of these properties (Figures 4 – 7 (e), (f) and (g) respectively), we require that at least three of the four  $H_2$  S(2) – S(5) rotational emission lines have a signal-to-noise ratio greater than 3 and that the line established by the fit falls within the  $1\sigma$  error bars of all three of the measurements. Due to the lack of LL coverage in our sample and the low statistical weight of the S(0) line, establishing the temperature,  $N_{H_2}$ , and  $R_{OP}$  of the cool  $H_2$  is not possible except in NGC 2023N and a limited portion of NGC 7023.

### 3.3.1. $H_2$ S(4) Overestimation

In NGC 7023 and NGC 2023,  $H_2$  S(4) consistently falls above the fit defined by S(2), S(3) and S(5). We determined that this is due to the S(4) line, at  $8.06 \mu\text{m}$ , overlapping the broad  $7.7 \mu\text{m}$  PAH feature. The  $H_2$  features in both of these PDRs are weak compared to the PAH emission (see Figure 4 – 6 (a) and (b)) and the PAHFIT routine overestimates the S(4) flux in these two PDRs by  $\sim 10\text{-}50\%$ . This error causes an overestimation of the  $H_2$  temperature of  $\sim 30$  K and  $N(H_2)$  of  $\sim 10\%$ . For each PDR, we used our temperature

fit to the S(2), S(3) and S(5) lines to estimate the actual S(4) flux and then applied the average overestimation, relative to the PAH 7.7  $\mu\text{m}$  flux, as a correction to the S(4) flux for the entire PDR. This correction was necessary as the S(5) line is weaker than the S(4) line in these PDRs and not always detected.

The ortho-to-para ratio is much more sensitive to the S(4) overestimation than the temperature or column density. While our correction does improve the quality of the  $R_{OP}$  fit, it also introduces an additional degree of uncertainty, therefore we do not use H<sub>2</sub> S(4) to estimate ortho-to-para ratios. We utilize all S(2) - S(5) rotational lines to fit a temperature (which simultaneously fits an ortho-to-para ratio) and then we remove the S(4) line, set the temperature and column density, and determine the best fit ortho-to-para ratio to the remaining lines. This significantly reduced the scatter of the ortho-to-para maps (Figures 4 – 6 (g)). IC 63, which has lower total PAH flux relative to H<sub>2</sub> emission (Figures 7 (a) and (b)), does not show evidence of H<sub>2</sub> S(4) overestimation.

### 3.4. $G_o/n_H$

The gas temperature and the ionization state of PAHs can be used as a probe of the local density and UV field strength,  $G_o/n_H$ . Using the parameter fit for the 11.3  $\mu\text{m}$  flux ratio of ionized to neutral PAHs ( $I_{11.3}^+/I_{11.3}^0 \sim 0.6$ ) and Equation [2] from Joblin et al. (1996),

$$\frac{I_{7.7\mu\text{m}}}{I_{11.3\mu\text{m}}} = 1.3 \left( \frac{1 + 5.54 \frac{PAH^+}{PAH^0}}{1 + 0.6 \frac{PAH^+}{PAH^0}} \right), \quad (4)$$

where  $PAH^+$  and  $PAH^0$  represent the total number of ionized and neutral PAHs respectively. This equation can be related to  $\sqrt{T_{gas}} G_o/n_e$  by solving for the neutral fraction,  $f_n = PAH^0/(PAH^+ + PAH^0)$ , and setting it equal to the ionization parameter relation,  $f_n =$

$(1+\gamma_o)^{-1}$  (Bakes & Tielens 1994; Tielens 2005).

$$\gamma_o = 3.5 \times 10^{-6} N_C^{\frac{1}{2}} \frac{G_o T^{1/2}}{n_e}, \quad (5)$$

$$\left( \frac{I_{7.7}/I_{11.3} - 1.3}{7.2 - 0.6(I_{7.7}/I_{11.3})} \right) \approx 3.5 \times 10^{-6} N_C^{\frac{1}{2}} \left( \frac{G_o \sqrt{T_{gas}}}{n_e} \right). \quad (6)$$

We adopt an average number of carbons atoms per PAH of  $N_C = 50$ . This approximation breaks down near the total ionization limit of  $I_{7.7}/I_{11.3} \rightarrow 12$ , however we do not encounter  $I_{7.7}/I_{11.3} > 11$  except in NGC 7023 in the inner nebular regions near HD 200775. We do not include data from that region in the following analysis. We estimate the electron density,  $n_e$  by assuming that all free electrons come from singly ionized gaseous carbon, and that all atomic carbon in the PAH emission region is ionized. Using the C/H ratio from Sofia (2004), the electron density is estimated to be  $n_e \approx 1.6 \times 10^{-4} n_H$ . Maps of  $G_o/n_H$  are presented in Figures 4 (h) – 7 (h).

## 4. Results

### 4.1. NGC 7023

In Figures 4 (a) and (b) it is clear that the PAHs and  $H_2$  do not share the same morphology. The PAHs extend  $\sim 20''$  closer to HD 200775 than the  $H_2$ , which rapidly falls from its peak at the starwards edge of the ribbon feature. Figure 9 shows that the PAH emission peaks on average  $\sim 1.5''$  starwards of the  $H_2$ . The separation of  $H_2$  rotational emission and PAHs has been shown before, most notably across the Orion Bar (Tielens et al. 1993; Kassis et al. 2006), however in PDRs with weaker UV fields this has not been observed (Compi gne et al. 2007).

#### 4.1.1. PAH Band Ratios

Figure 4 (c) shows that the PAH band ratio  $I_{7.7}/I_{11.3}$  is at a minimum near the bright ribbon feature and increases with decreasing projected distance to HD 200775. This is consistent with the findings of Rapacioli et al. (2005), who used *ISO* spectra to show that the relative contribution to the PAH spectrum of ionized PAHs increases closer to the central star. The geometry of the band ratio map does not match any of the other MIR observables and we note no apparent correlation between total PAH emission and ionization until  $I_{7.7}/I_{11.3} \sim 8$ . At this ratio, which from Equation [4] indicates an ionization fraction of  $f_+ \sim 0.74$ , the total PAH flux begins to rapidly decline, potentially indicating destruction, falling by more than half over  $\sim 5''$  (Figure 9).

The dehydrogenation ratio  $I_{12.7}/I_{11.3}$  is highest both in the bright ribbon feature and close to HD 200775 (Figure 4 (d)). Beginning at the starwards edge of the dissociation front and extending  $\sim 10''$  towards the central star there is a trough where the ratio reaches a minimum. As with the ionization ratio, the geometry does not follow that of any other observable.

#### 4.1.2. $H_2$ Features

The increase in  $H_2$  column density (Figure 4 (e)) and flux at the bright ribbon feature is likely due to the onset of  $H_2$  self-shielding, which is a rapid process. In the ribbon feature the  $R_{OP}$  of the  $H_2$  is a nonequilibrium value of  $\sim 1.83 \pm 0.51$ , which is consistent with the  $\sim 2$  reported in Fuente et al. (2000). We note a spike in the ratio to values  $> 3$  near the starward edge of the dissociation front which is possibly the result of the greater ability of ortho- $H_2$  to self-shield (Draine & Bertoldi 1996). This measurement is not statistically significant, however, and is consistent with an  $R_{OP} = 3$ .

We observe a small but still significant separation of ortho- and para-H<sub>2</sub>  $\sim 2''$ , which is shown in Figure 10. Between 30-40'' from HD 200775 there is an increase in  $R_{OP}$  which occurs at the HI/H<sub>2</sub> transition. While the detection of  $R_{OP} > 3$  in NGC 7023 is not statistically significant, these profiles and the  $R_{OP}$  spike suggest that we are observing the effects of preferential self-shielding of ortho-H<sub>2</sub>. If this interpretation is correct, it would be the first detection of the effects of preferential self-shielding of ortho-H<sub>2</sub> in a PDR.

The bright ribbon of NGC 7023 has been a target of numerous H<sub>2</sub> studies from the far-UV (France et al. 2006, 2009) to the NIR (Lemaire et al. 1996; Takami et al. 2000) and MIR (Fuente et al. 2000), however to our knowledge this work is the first to derive properties of H<sub>2</sub> emission between the dissociation front and HD 200775, where the gas is subject to a harsher UV radiation field and higher  $G_o/n_H$  (Figure 4 (h)). Previous H<sub>2</sub> 1-0 S(1) and other narrow band imaging (Lemaire et al. 1996; Takami et al. 2000) failed to detect any H<sub>2</sub> emission in this region. Fuente et al. (2000) reported a weak 0-0 S(1) detection with *ISO*, however they did not detect any other rotational lines at that location. We find that the IRS SL band H<sub>2</sub> in this region is generally hotter ( $\sim 1000\text{K}$ ), at nearly an order of magnitude lower  $N_{H_2}$  ( $N_{H_2} \sim 1 \times 10^{19} \text{ cm}^{-2}$ ), and close to an  $R_{OP}$  of 3.

Previous MIR studies of NGC 7023 with *ISO* (Fuente et al. 2000; Rapacioli et al. 2005) and *Spitzer* (Berné et al. 2007) have indicated a warm-H<sub>2</sub> at  $T_{gas} \sim 400 - 700\text{K}$  and  $N_{H_2} \sim 10^{20} \text{ cm}^{-2}$ . These values are not matched by those listed in Table 3, however the data in the table is skewed by giving equal weight to  $T_{gas}$  and  $N_{H_2}$  calculated for the H<sub>2</sub> starwards of the bright emission ribbon. When the flux of each rotational line over the entire observing area is rebinned into a single value, which is dominated by flux from the ribbon, we calculate a  $T_{gas} \sim 650\text{K}$ ,  $N_{H_2} \sim 6 \times 10^{19} \text{ cm}^{-2}$ , and  $R_{OP} \sim 1.83$ . These values are in line with previous work.

## 4.2. NGC 2023 North

The PAH emission in NGC 2023N peaks  $\sim 10''$  away from the peak of the total detected SL band  $\text{H}_2$  emission. The separation is more pronounced between the PAHs and emission from the para- $\text{H}_2$  states (including S(0)) than the ortho- $\text{H}_2$  states (including S(1)). This can be seen by noting that the  $R_{OP}$  peak in Figure 5 (g) is closer to the PAH emission peak in Figure 5 (a) than the  $\text{H}_2$  peak in Figure 5 (b). This indicates that the direction of the advancing photodissociation front is moving from the lower right of the maps towards the upper left, even though HD 37903 is located closer to the bottom left.

### 4.2.1. PAH Features

The PAH ionization and dehydrogenation relations in Figures 5 (c) and (d) both reach a minimum near the PAH emission peak and increase with decreasing PAH emission. The low  $I_{7.7}/I_{11.3}$  values indicate that the PAHs are primarily neutral throughout the observed area. It is likely that the slight increase in PAH ionization to the north of the dissociation front in NGC 2023N is due to a decreasing  $n_H$  and relatively flat  $G_o$ , therefore increasing the ratio  $G_o/n_H$  as seen in Figure 5 (h).

### 4.2.2. $\text{H}_2$ Features

NGC 2023N is also a well studied PDR, with observations from the FUV (Burgh et al. 2002; France et al. 2009) to the NIR (Hasegawa et al. 1987; Gatley et al. 1987; Takami et al. 2000). Unlike NGC 7023, we calculate a nearly flat and featureless gas temperature and only a factor of  $\sim 2$  drop in  $N_{\text{H}_2}$  outside of the  $\text{H}_2$  bright ribbon (Figures 5 (f) and (e)). When all of the SL band  $\text{H}_2$  is summed, as in Figure 5 (b), the para- $\text{H}_2$  dominates the flux and  $N_{\text{H}_2}$ .



The separation between ortho- and para-H<sub>2</sub> is larger in NGC 2023N than in NGC 7023. Figure 11 shows a  $\sim 10''$  separation between the ortho- and para-H<sub>2</sub> peaks which exists not only in the SL band rotational lines (S(2) – S(5)), but also in the LL rotational lines S(0) and S(1). NGC 2023N is not oriented so that the projected vector towards the central star is perpendicular to the dissociation front, nevertheless Figures 5 (f), (g), and Figure 11 show that  $R_{OP}$  is nearly identical on either side of the  $R_{OP}$  peak and  $T_{gas}$  is flat throughout. This implies that collisional conversion has transitioned the  $R_{OP}$  from a formation value to  $\sim 1.25$  ( $R_{OP}$  calculated using only the S(0) and S(1) lines for  $T_{gas} = 200$  K is 0.67), and that the passing of the dissociation front is causing a temporary peak in  $R_{OP}$  by preferential self-shielding of the ortho-H<sub>2</sub> in both the cool, diffuse gas and the warm, dense clumps simultaneously.

### 4.3. NGC 2023 South

NGC 2023S contains a bright emission ridge  $\sim 78''$  south of HD 37903 which has been thoroughly studied from the far-UV (Burgh et al. 2002) to the radio (Steiman-Cameron et al. 1997) and has been used as a template for modeling of dissociation fronts (Draine & Bertoldi 1996). The ridge area is considered to be denser ( $\sim 10^5$  cm<sup>-3</sup>) and have a slightly more thermal H<sub>2</sub> vibrational spectrum than its northern counterpart. The NGC 2023S IRS coverage extends over a significantly broader area than the bright emission ridge, however, extending up to  $\sim 15''$  from HD 37903 to as far as  $100''$  away.

The H<sub>2</sub> and PAH emission in Figures 6 (a) and (b) both are at a maximum in the bright emission ridge centered at approximately [0,-20]. As with NGC 7023, the PAH emission remains nearer to its peak flux level at smaller projected distances to the central star than the H<sub>2</sub>. Figure 12 shows that the PAH emission peak precedes the H<sub>2</sub> emission peak in the bright ridge, as it did in NGC 2023N and NGC 7023, but by only  $\sim 0.6''$ , which

is not statistically significant. Higher resolution measurements would be needed to confirm this separation.

#### 4.3.1. PAH Features

The PAH ionization band ratio  $I_{7.7}/I_{11.3}$  in the bright emission ridge is at a similar average value ( $I_{7.7}/I_{11.3} \sim 3$ ,  $f_+ \sim 0.25$ ) to the ratio in the ribbon of NGC 7023. To the north of the emission ridge the ratio increases to a maximum value of just less than 7, indicating an ionization fraction of  $f_+ \sim 0.65$ . In the mapped region closest to HD 37903, however, the PAH ionization level drops, possibly due to the complex geometry of NGC 2023S resulting in foreground or background contributions to the PAH emission.

The PAH dehydrogenation band ratio map (Figure 6 (d)) may be contaminated by the presence of a bright star at the bottom edge of the mapped area. The star and another fainter one to the north were removed to avoid contamination, however at  $12.7 \mu\text{m}$  some contamination still exists. The concentric rings around the blacked out area in Figure 6 (d) suggest that this may be affecting the measurement. In the northern part of the map we observe values similar to NGC 7023 and NGC 2023N with slightly higher ratios nearer to the central star.

#### 4.3.2. $H_2$ Features

The bright emission ridge coincides with the highest  $N_{H_2}$  in NGC 2023S ( $N_{H_2} \sim 1.87 \pm 0.30 \times 10^{20} \text{ cm}^{-2}$ , Figure 6 (e)). Within this region the temperature averages  $\sim 625 \pm 13\text{K}$  with an  $R_{OP} \sim 1.87 \pm 0.1$ . The spread on the values cited represent the standard deviation within the region, not the error on the measurements. We cite standard deviations here to show the relative homogeneity of of the observations within the regions discussed in this

section. Farther to the south of the ridge,  $N_{H_2}$  drops off slightly to  $\sim 8.9 \pm 3.5 \times 10^{19}$   $\text{cm}^{-2}$ , while  $T_{gas}$  ( $592 \pm 32\text{K}$ ) and  $R_{OP}$  ( $1.7 \pm 0.2$ ) remain at levels similar to those within the emission ridge. In the top left portion of the maps, nearest to HD 37903 and coincident with the area where we noted a drop in  $I_{7.7}/I_{11.3}$  in §4.3.1,  $N_{H_2}$ ,  $T_{gas}$  and  $R_{OP}$  are all consistent with the values in the southern portion of the map ( $T_{gas} \sim 575 \pm 42\text{K}$ ,  $N_{H_2} \sim 6.9 \pm 1.6 \times 10^{19}$   $\text{cm}^{-2}$ ,  $R_{OP} \sim 1.63 \pm 0.41$ ). The similarity in these properties suggests that the gas dominating the emission in the upper left may be a foreground or background portion of NGC 2023S enveloping the central cavity.

North-west of the dissociation front,  $N_{H_2}$  drops by over an order of magnitude relative to the ridge feature ( $N_{H_2} \sim 1.9 \pm 1.4 \times 10^{19}$   $\text{cm}^{-2}$ ). The corresponding increase in  $T_{gas}$  to  $\sim 847 \pm 325\text{K}$  suggests that the  $\text{H}_2$  in this region of NGC 2023S is similar to the  $\text{H}_2$  starwards of the dissociation front in NGC 7023. The increased PAH ionization fraction and higher  $G_o/n_H$  in Figure 6 (h) also follow the PAH behavior starwards of the dissociation front in NGC 7023.  $R_{OP}$ , however, rather than increasing to the LTE  $R_{OP} \sim 3$ , falls to extremely low values  $\sim 0.6 \pm 0.22$ . This unusual observation will be discussed further in § 5.3.1.

#### 4.4. IC 63

IC 63 features the weakest PAH and  $\text{H}_2$  flux in our sample and the lowest ratio of PAH flux to  $\text{H}_2$  flux (Figure 7 (a) and (b)). We detect no statistically significant separation of the PAH and  $\text{H}_2$  emission in IC 63 (Figure 13). We also calculate the lowest average  $I_{7.7}/I_{11.3}$  ratio in our sample with an estimate ionization fraction of  $f_+ \sim 0.082$ . This ratio does not reach the average values observed in the other PDRs anywhere in the observed region (Figure 7 (c)). It is worth noting that IC 63 is at a larger distance from the exciting star  $\gamma\text{-Cas}$  ( $\sim 1.3$  pc) than NGC 2023 ( $\sim 0.33$  pc to NGC 2023N) and NGC 7023 ( $\sim 0.1$

pc), therefore  $G_o$  is lower due to geometric effects despite the harder radiation spectrum from the B0 star. Figure 7 (d) shows that the dehydrogenation relation  $I_{12.7}/I_{11.3}$  is mostly constant, however there is a decrease in the ratio near the starward edge of the PDR. We will investigate this further in §5.1.2.

The temperature, column density, and  $G_o/n_H$  all fluctuate only moderately (Figures 7 (e), (f) and (h)). The average measured  $T_{gas}$  of  $\sim 625\text{K}$  is consistent with the temperature cited in Habart et al. (2004) and Karr et al. (2005) ( $T_{gas} = 630\text{K}$ ). IC 63 was the subject of an extensive multiwavelength study in Karr et al. (2005) in which *ISO* MIR data was used to compute temperatures and column densities, as well as to compare PAH band ratios. They reported a nearly flat PAH  $I_{11.3}/I_{6.2}$  band ratio, a probe of PAH ionization, which is in good agreement with the low variation of  $I_{7.7}/I_{11.3}$  shown in Figure 7 (c). They calculate an average  $I_{11.3}/I_{6.2} \sim 2$ , however, which is twice the average that we calculate for this PDR ( $I_{11.3}/I_{6.2} \sim 0.93$ ), and would indicate even less PAH ionization if correct. The  $R_{OP}$  in Figure 7 (g) peaks at a nearly LTE value at the starwards edge of IC 63 before moderating down to  $\sim 1.5$  at the back edge of our observing region. This implied trend in  $R_{OP}$  can only be confirmed with a more extended coverage area, however it is consistent with an advancing photodissociation front.

## 5. Discussion

In this section, we address connections that can be made between the properties that we have observed in these PDRs. We address the limited understanding of the dehydrogenation relation and reference a proposed  $\text{H}_2$  formation scenario which may explain the observed band variations. We also consider whether our calculation of  $G_o/n_H$  is a valid one given that the dominant  $\text{H}_2$  emission in the IRS SL bandpass is from warm, dense gas clumps whereas the dominant PAH emission may not be. We conclude by analyzing

our ortho-to-para ratio maps and how observed trends fit with current understanding of advancing dissociation fronts.

## 5.1. PAH Dehydrogenation

### 5.1.1. NGC 7023 and NGC 2023

In NGC 7023, NGC 2023N, and NGC 2023S, we observe an increase in the PAH dehydrogenation relation,  $I_{12.7}/I_{11.3}$ , beginning within the bright  $H_2$  ribbons and increasing slightly with greater distance from the central stars. This increase indicates that the PAHs are being stripped of hydrogen atoms despite corresponding drops in the ionization relation,  $I_{7.7}/I_{11.3}$ , and  $G_o/n_H$  (Figures 4, 5, 6 (c), (h)). In all three PDRs,  $I_{12.7}/I_{11.3}$  reaches a minimum, indicating the peak of PAH hydrogenation, just starwards of the  $H_2$  peak, where the  $H_2$  is dissociating. The  $I_{12.7}/I_{11.3}$  relation then increases again nearest the central stars in NGC 7023 and NGC 2023S. This effect is illustrated in Figure 14, which shows the averaged profiles of  $I_{12.7}/I_{11.3}$  and  $N(H_2)$  with respect to HD 200775 in NGC 7023. The corresponding drop in total PAH emission near HD 200775 seen in Figure 9 may be evidence of the evaporating of PAH molecules due to a higher  $G_o/n_H$  and ionization fraction. This would be consistent with previous results showing that PAH ionization precedes dissociation in the reflection/emission nebula IC 405 (France et al. 2007).

The PAH dehydrogenation in the molecular layer may be due to a different process.  $H_2$  formation on PAH surfaces has been proposed as a dominant formation process in high temperature PDRs (Habart et al. 2004), overtaking the traditional ISM formation process between physisorbed H atoms on grain surfaces, which is effective only at low temperatures. Le Page et al. (2009) propose a formation mechanism where an ionized, fully hydrogenated PAH encounters an H atom and becomes overly hydrogenated (the gas phase hydrogen

atom becomes bound to the surface of the PAH) and then recombines with a free electron, which dislodges either the extra H atom or an H<sub>2</sub> molecule. In the H<sub>2</sub> ejection scenario, the neutral PAH product would be left with one fewer hydrogen atom than it had previously, and thus is dehydrogenated. The observed increase in  $I_{12.7}/I_{11.3}$  may indicate the presence of dehydrogenated PAHs due to an ongoing H<sub>2</sub> formation process.

Neither PAH destruction nor H<sub>2</sub> formation fully explains the decrease in  $I_{12.7}/I_{11.3}$  just starwards of the dissociation front, which is most easily seen in NGC 7023 (Figure 4 (d)). This region has a higher PAH ionization fraction than in the molecular layer, which is an important catalyst for most H<sub>2</sub> formation scenarios on PAH surfaces (Bauschlicher 1998; Pauzat & Ellinger 2001; Le Page et al. 2003), therefore we would expect the formation rate to increase as more PAH cations become available. If the dehydrogenation ratio in the molecular layer is due to H<sub>2</sub> formation, then the lower  $I_{12.7}/I_{11.3}$  starwards of the dissociation front would indicate a quenching of that process.

### 5.1.2. PAH Destruction in IC 63

We detect no significant variation of  $I_{12.7}/I_{11.3}$  in the emission nebula IC 63 other than a minimum near the southern starwards edge (Figure 7 (d)). This region corresponds the highest  $R_{OP}$  in IC 63, suggesting selective self-shielding of ortho-H<sub>2</sub> and therefore an HI/H<sub>2</sub> transition layer. A dehydrogenation minimum near the leading edge of the HI/H<sub>2</sub> transition is consistent with observations in NGC 7023 and NGC 2023. IC 63 also exhibits FUV H<sub>2</sub> fluorescence indicative of very little extinction between the PDR and  $\gamma$ -Cas (Witt et al. 1989; France et al. 2005) and the PAH emission region has been shown to be enveloped in an ionized atomic layer  $\sim 0.002$  pc thick (Karr et al. 2005; France et al. 2005). That the PAH emission does not continue into the HII region traced by H $\alpha$  indicates that the PAH molecules are being dissociated near the starwards edge of the PDR. Figure 7 (d), however,

does not show any evidence of an increase in the dehydrogenation relation, suggesting that either that the dissociation is happening too quickly to be resolvable or that the dehydrogenation signature is too weak to detect. PAH molecules can be dissociated directly by the absorption of single high energy photons, however the required photon energy increases with the number of carbon atoms in the core, with a PAH of  $N_C = 50$  requiring an EUV photon of  $\sim 24$  eV (Siebenmorgen & Krügel 2010). Recent studies have shown that  $\gamma$ -Cas is a soft x-ray emitter (Lopes de Oliveira et al. 2010), making single photon dissociation a possible scenario.

The average value of the  $I_{12.7}/I_{11.3}$  dehydrogenation ratio in IC 63 is similar to the average in the H<sub>2</sub> bright ribbons of NGC 2023 and NGC 7023 ( $\sim 0.41$ ), suggesting that the same processes that influence this ratio are occurring in all four PDRs. The ionization relation however (Figure 7 (c)), indicates that IC 63 is very close to the PAH neutral limit of  $I_{7.7}/I_{11.3} \sim 1.3$ , limiting the number of PAH cations available for H<sub>2</sub> formation.

## 5.2. Reconciliation of $G_o/n_H$

To calculate  $G_o/n_H$  we have used the PAH 7.7  $\mu\text{m}$  and 11.3  $\mu\text{m}$  flux in conjunction with the temperature of the warm H<sub>2</sub> component, which represents  $\sim 1\%$  of the total H<sub>2</sub> column (Figure 8). This method has been used before (Galliano et al. 2008; Berné et al. 2009), however it assumes that the PAH ionization relation is independent of the local hydrogen density. In our example, where we have used the warm H<sub>2</sub> temperature to calculate  $G_o/n_H$ , we are assuming that we are calculating the ratios within those dense gas clumps.

Radio observations of PDRs often use other molecules, such as CO, as a proxy for H<sub>2</sub> (Chokshi et al. 1988). These studies predict H<sub>2</sub> temperatures for the low density, cool H<sub>2</sub> component ( $n_H \sim 10^3 \text{ cm}^{-3}$ ,  $T_{gas} \sim 100\text{K}$ ), while MIR studies of the warm, dense H<sub>2</sub>

clumps have indicated densities  $\sim 10^4 - 10^5 \text{ cm}^{-3}$  and temperatures  $\sim 600\text{K}$ . For these cases, the difference in temperature,  $\sqrt{T_{warm}/T_{cool}} \sim 2.5$ , does not account for the order of magnitude or more difference in  $n_H$  using the equations in §3.4.

In order for the actual value calculated to be the correct  $G_o/n_H$  within the warm, dense  $\text{H}_2$  clumps that we are studying, the PAH flux must be dominated by emission from within those same high density clumps, thereby probing the same environment as the warm  $\text{H}_2$  temperature that we are using. If this is not the case, then either  $G_o$  is larger within the high density clumps than in the low density, cool component, or we are improperly using the warm  $T_{gas}$  and obtaining an incorrect measure of  $G_o/n_H$ . We therefore caution that our maps of  $G_o/n_H$  be used primarily as a measure of the variation of the ratio over the PDR, and not as a means of obtaining an absolute value for a specific portion of the PDR.

### 5.3. $\text{H}_2$ Ortho-Para Ratio

The formation ratio of ortho- to para- $\text{H}_2$  ( $R_{OP}$ ) in a warm gas ( $T_{gas} \geq 250 \text{ K}$ ) is expected to be 3.  $\text{H}_2$  that forms at a cooler temperature will have a lower  $R_{OP}$  as more  $\text{H}_2$  is formed in the  $J = 0$  para-rotational state. Subsequent radiative heating of the gas allows  $J$  to change by only  $\pm 2$ , thus the formation  $R_{OP}$  is preserved in higher  $J$  rotational states. Radiative processes cannot convert ortho- $\text{H}_2$  to para- $\text{H}_2$ , however the total nuclear spin can be altered by collisions with  $\text{H}$  and  $\text{H}^+$  atoms, which moves  $R_{OP}$  towards the local thermal equilibrium value defined by the new temperature (Sternberg & Neufeld 1999).

The observed  $R_{OP}$  for a temperature,  $T_{gas}$ , and density of atomic hydrogen,  $n_{HI}$ , after a time  $\tau$  can be predicted by Equation [2] from Neufeld et al. (2006). Assuming a  $T_{gas} \sim 650\text{K}$ , a density of  $n_H \sim 10^5$ ,  $n_{HI} = 10^{-3}n_H$ , and an initial ortho-to-para ratio of  $R_{OP_o} = 0.75$  (corresponding to a formation temperature  $\sim 50 - 75\text{K}$ ), the observed  $R_{OP}$  after 5000



years at  $T_{gas}$  should be  $\sim 2.15$ . This is within the  $1\sigma$  errors of the average  $R_{OP}$  we measure for the ribbon of NGC 7023 ( $1.86 \pm 0.32$ ), which has been exposed to HD 200775 for  $\sim 5000$  years (Rogers et al. 1995). It is also consistent with IC 63 ( $R_{OP} = 1.99 \pm 0.37$ ) which has similar  $T_{gas}$  and  $n_H$ .

A PDR with a moving dissociation front should exhibit a gradient in both the temperature and  $R_{OP}$  as the front advances into the cool, low  $R_{OP}$  gas, heats it, and begins the para  $\rightarrow$  ortho conversion. This process is most clearly observed in NGC 7023 in Figures 4 (f) and (g), where the cool, outer regions of the PDR have a lower  $R_{OP}$  than nearer to the central star, where  $R_{OP}$  is closer to 3. It is also apparent in Figure 10 where beyond the  $H_2$  emission peak  $R_{OP}$  falls to  $\sim 0.6$ , reflecting a low formation temperature, while  $T_{gas}$  levels out, indicating recent heating. We also observe a spike in  $R_{OP}$  at the starwards edge of the dissociation front in NGC 2023N, however the measured values do not exceed 3. There is also the possibility that the  $R_{OP} \sim 3$  closest to HD 200775 in NGC 7023 is the result of rapid dissociation and formation processes and the relatively small amount of  $H_2$  detected in that region is newly formed  $H_2$ , not relic  $H_2$  which has transitioned to LTE.

All four PDRs studied in this paper exhibit non-equilibrium ortho-to-para ratios which indicate that the  $H_2$  formed at much lower temperatures prior to illumination by the central stars. The ortho-to-para ratios in IC 63 and NGC 7023 generally follow expectations for a recently heated PDR, however more coverage area in IC 63 is needed to confirm the implied trends in Figure 7 (g).

### 5.3.1. *Extremely Low $R_{OP}$ in NGC 2023 South*

In NGC 2023S we calculate very low non-equilibrium ortho-to-para ratios within a pocket of warmer, low  $N(H_2)$  gas at a smaller projected distance to the central star than

the bright emission ridge (Figure 6 (g)). Ratios in this region, where the temperature occasionally exceeds 1000K, fall to  $< 1$  with an average of  $0.6 \pm 0.22$ . At such high temperatures the para  $\rightarrow$  ortho conversion process should bring the gas to almost LTE within 1000 years and to  $R_{OP} > 1$  within a few hundred years for  $n_H \sim 5 \times 10^4 \text{ cm}^{-3}$  (Neufeld et al. 2006). We know of only two scenarios which could explain such extreme values. Either the gas has only been recently and rapidly heated, or the density of the gas is significantly lower than in the rest of the PDR, slowing the transition process. This region coincides with the highest  $G_o/n_H$  in NGC 2023S (Figure 6 (h)), implying either a strong UV radiation field or a low density. Such low ortho-to-para ratios for warm ( $T_{gas} \geq 500\text{K}$ ) have been reported in Neufeld et al. (2006) and Maret et al. (2009), however only for gas recently heated by a passing shock wave. This region merits further study to better understand and confirm these results.

## 6. Conclusions

In the photodissociation regions near hot stars, the MIR spectrum is dominated by emission from PAHs and the pure rotational lines of  $\text{H}_2$ . We have shown that while these two species are independent of each other, they provide complementary diagnostic tools to probe the environment of the PDR. Utilizing the spatial and spectral capabilities of the *Spitzer Space Telescope*, we have created spectral maps of the ortho-to-para ratio, temperature, column density of  $\text{H}_2$ ,  $G_o/n_H$ , PAH ionization, and a measure of the PAH surface structure. These diagnostics, combined with spectral mapping techniques, enable the study of PDR environments on angular scales of a few arcseconds. Such maps will prove valuable to future spectral mapping studies with *Herschel*, which does not have direct access to the bulk of the PDR gas mass ( $\text{H}_2$ ) in its far-infrared and sub-mm bandpasses.

### 6.1. PAH Features

Using the PAH emission in the MIR, we were able to establish an estimate of  $\sqrt{T_{gas}} G_o/n_H$  across the entire coverage region using the  $I_{7.7\mu m}/I_{11.3\mu m}$  C-C/C-H band ratio. There is evidence for PAH dehydrogenation, and possibly destruction, in NGC 7023 at radii  $< 30''$  ( $\sim 0.058$  pc) from HD 200775. The onset of PAH dehydrogenation in NGC 7023 coincides with a drop in PAH intensity in every band and an ionization fraction of  $f_+ \sim 0.74$ . At projected distances  $> 30''$  the dehydrogenation ratio reaches a minimum before increasing again in the H<sub>2</sub>/PAH bright ribbon feature. The dehydrogenation signature in the molecular layer may indicate that H<sub>2</sub> is forming on the PAH surfaces, and that the process is removing a bound hydrogen atom from the PAH. We find that in all three PDRs,  $I_{12.7}/I_{11.3}$  peaks where  $T_{gas} \sim 600$ -700K, possibly indicating the peak efficiency temperature for H<sub>2</sub> formation on PAH grain surfaces.

In three of the four PDRs studied, the PAH emission peaks a few arcseconds closer to the central star than the H<sub>2</sub> emission. The projected separation distance varied from  $\sim 0.6''$  and  $1.5''$  in NGC 2023S and NGC 7023 respectively, to  $\sim 10''$  in NGC 2023N. In IC 63, no separation was observed between H<sub>2</sub> and PAH features, however the weak  $G_o/n_H$  of IC 63 or the viewing geometry may make the separation unresolvable. In NGC 2023N we observed no significant separation between the PAHs and the ortho-H<sub>2</sub>, however the para-H<sub>2</sub> dominates the total H<sub>2</sub> emission and column density in this PDR. This may also be the case in NGC 7023 where an ortho- and para-H<sub>2</sub> separation was observed of similar magnitude ( $\sim 2''$ ) to the PAH-H<sub>2</sub> total separation. We lack the resolution to definitively determine if the ortho-H<sub>2</sub> is cospatial with the peak PAH emission in this PDR. No separation between ortho- and para-H<sub>2</sub> was detected in NGC 2023S, although there is a suggestion of a PAH-H<sub>2</sub> separation of  $\sim 0.6''$ , although it is not statistically significant. Higher spatial resolution measurements are required to confirm a separation.

## 6.2. H<sub>2</sub> Features

Despite the strong PAH features in these PDRs, we were able to construct spectral line maps of multiple H<sub>2</sub> emission lines. We fit gas temperatures of the warm H<sub>2</sub> component which closely match global H<sub>2</sub> derived temperatures from previous studies, but with the added benefit of spatial resolution. Due to the strength of the PAH features, we were unable to accurately fit the H<sub>2</sub> S(4) and S(6) rotational lines in NGC 2023 and NGC 7023, however we estimate that the error introduced to the S(4) flux is negligible in IC 63. For the purposes of temperature and column density calculations we applied a correction to the S(4) flux to increase our spatial coverage area.

In the bright emission ridges of NGC 7023 and NGC 2023N the ortho-rotational emission peaks before the para-rotational H<sub>2</sub>; an effect most pronounced in NGC 2023N and not detected in IC63 and NGC 2023S. In NGC 2023N, where we had complete complementary IRS LL data, the peak of the ortho-to-para ratio calculated for the cool, low density H<sub>2</sub>, defined by the S(0) and S(1) emission lines, is cospatial with the peak of the ortho-to-para ratio for the warm, dense clumps; suggesting that H<sub>2</sub> self-shielding occurs at the same location regardless of the density or temperature phase of the H<sub>2</sub> gas.

We presented evidence of the preferential self-shielding of ortho-H<sub>2</sub> in both NGC 7023 and NGC 2023N. We also detected an implied trend in the ortho-to-para ratio in IC 63, with near LTE values at the leading edge of the PDR falling to  $\sim 1.5$  at the edge of our coverage area. In NGC 7023 we measured  $R_{OP} > 3$  (Figure 4 (g)), however the measurements are not statistically significant and are consistent with the LTE value of  $R_{OP} = 3$ . Ortho- and para-H<sub>2</sub> emission profiles in NGC 2023N and NGC 7023 (Figures 11 and 10) show that in both PDRs the ortho-H<sub>2</sub> emission peaks starwards of the para-H<sub>2</sub> emission profile, which supports a preferential self-shielding scenario. In NGC 2023N, we observe no lasting effect of preferential self-shielding of ortho-H<sub>2</sub> on  $R_{OP}$ , as  $R_{OP}$  was nearly identical on either side

of the dissociation front. The ortho-to-para ratio of the cool H<sub>2</sub> component in NGC 2023N is consistent with an initial formation temperature of 50 - 75K.

The authors would like to thank Dr. David Neufeld for helpful discussions and advice. We would also like to thank the anonymous referee for their helpful comments. This work is based in part on archival data obtained with the *Spitzer Space Telescope*, which as operated by the Jet Propulsion Laboratory, California Institute of Technology under a contract with NASA. Support for this work was provided by an award issued by JPL/Caltech for proposal ID: 30696.

## REFERENCES

- Allamandola, L. J., Hudgins, D. M. & Sandford, S. A. 1999, *ApJ*, 511, L115
- Bakes, E. L. O. & Tielens, A. G. G. M. 1994, *ApJ*, 427, 822
- Bakes, E. L. O. & Tielens, A. G. G. M. 1998, *ApJ*, 499, 258
- Bauschlicher, Jr., C. W., 1998, *ApJ*, 509, 125
- Berné, O., Joblin, C., Deville, Y., Smith, J. D., Rapacioli, M., Bernard, J. P., Thomas, J., Reach, W. & Abergel, A. 2007, *A&A*, 469, 575
- Berné, O., Fuente, A., Goicoechea, J. R., Pilleri, P., González-García, M. and Joblin, C. , 2009, *ApJ*, 706, 160
- Burgh, E. B. and McCandliss, S. R. and Feldman, P. D. , 2002, *ApJ*, 575, 240
- Chokshi, A., Tielens, A. G. G. M., Werner, M. W. & Castelaz, M. W. 1988, *ApJ*, 334, 803
- Compiègne, M., Abergel, A., Verstraete, L., Reach, W. T., Habart, E., Smith, J. D., Boulanger, F. and Joblin, C., 2007, *A&A*, 471, 205
- de Boer, K. S. 1983, *A&A*, 125, 258
- Draine, B. T. & Bertoldi, F. 1996, *ApJ*, 468, 269
- Draine, B. T. & Bertoldi, F. 2000, "Molecular Hydrogen in Space", 131
- Duley, W. W. and Williams, D. A. 1981, *MNRAS*, 196, 269
- Field, G. B., Somerville, W. B. & Dressler, K. 1966, *ARA&A*,4,207
- France, K. and Andersson, B.-G. and McCandliss, S. R. and Feldman, P. D., 2005, *ApJ*, 628, 750

- France, K., 2006, PhD Thesis
- France, K., McCandliss, S. R. and Lupu, R. E., 2007, *ApJ*, 655, 920
- France, K., McCandliss, S. R. and Burgh, E. B., 2009, American Institute of Physics Conference Series, 1135, 198
- Fuente, A., Martin-Pintado, J., Rodriguez-Fernández, N. J., Cernicharo, J. and Gerin, M., 2000, *A&A*, 354, 1053
- Galliano, F., Madden, S. C., Tielens, A. G. G. M., Peeters, E. & Jones, A. P. 2008, *ApJ*, 679, 310
- Gatley, I. and Hasegawa, T. and Suzuki, H. and Garden, R. and Brand, P. and Lightfoot, J. and Glencross, W. and Okuda, H. and Nagata, T. 1987, *ApJ*, 318, 73
- Habart, E., Boulanger, F., Verstraete, L., Walmsley, C. M. & Pineau des Forêts, G. 2004, *A&A*, 414, 531
- Habing, H. J. 1968, *Bull. Astron. Inst. Netherlands*, 19, 421
- Hasegawa, T. and Gatley, I. and Garden, R. P. and Brand, P. W. J. L. and Ohishi, M. and Hayashi, M. and Kaifu, N. 1987, *ApJ*, 318, 77
- Hollenbach, D. J. & Tielens, A. G. G. M. 1997, *ARA&A*, 35, 179
- Hony, S. and Van Kerckhoven, C. and Peeters, E. and Tielens, A. G. G. M. and Hudgins, D. M. and Allamandola, L. J. 2001, *A&A*, 370, 1030
- Hudgins, D. M. and Allamandola, L. J. 1999, *ApJ*, 516, 41
- Houck, J. R. et al. 2004, *SPIE*, 5487,62
- Jansen, D. J., van Dishoeck, E. F. and Black, J. H. , 1994, *A&A*, 282, 605

- Joblin, C., Tielens, A. G. G. M., Geballe, T. R. and Wooden, D. H., 1996, *ApJ*, 460, 119
- Karr, J. L., Noriega-Crespo, A. and Martin, P. G., 2005, *AJ*, 129, 954
- Kassis, M., Adams, J. D., Campbell, M. F., Deutsch, L. K., Hora, J. L., Jackson, J. M. and Tollestrup, E. V., 2006, *ApJ*, 637, 823
- Leger, A. & Puget, J. L. 1984, *A&A*, 137, L5
- Lemaire, J. L., Field, D., Gerin, M., Leach, S., Pineau des Forets, G., Rostas, F. and Rouan, D., 1996, *A&A*, 308, 895
- Le Page, V. and Snow, T. P. and Bierbaum, V. M., 2003, *ApJ*, 584, 316L
- Le Page, V., Snow, T. P. and Bierbaum, V. M., 2009, *ApJ*, 704, 274
- Li, A. and Draine, B. T. 2001, *ApJ*, 554, 778
- Lopes de Oliveira, R. and Smith, M. A. and Motch, C., 2009, *A&A*, 512, 22
- Maret, S., Bergin, E. A., Neufeld, D. A., Green, J. D., Watson, D. M., Harwit, M. O., Kristensen, L. E., Melnick, G. J., Sonnentrucker, P., Tolls, V., Werner, M. W., Willacy, K. and Yuan, Y., 2009, *ApJ*, 698, 1244
- Neufeld, D. A., Melnick, G. J., Sonnentrucker, P., Bergin, E. A., Green, J. D., Kim, K. H., Watson, D. M., Forrest, W. J. and Pipher, J. L., 2006, *ApJ*, 649, 816
- Pauzat, F. and Ellinger, Y., 2001, *MNRAS*, 324, 355
- Peeters, E. and Hony, S. and Van Kerckhoven, C. and Tielens, A. G. G. M. and Allamandola, L. J. and Hudgins, D. M. and Bauschlicher, C. W. 2002, *A&A*, 390, 1089
- Rapacioli, M., Joblin, C. and Boissel, P. 2005, *A&A*, 429, 193
- Rogers, C., Heyer, M. H. & Dewdney, P. E. 1995, *ApJ*, 442, 694



- Sellgren, K. and Werner, M. W. and Dinerstein, H. L., 1992, *ApJ*, 400, 238
- Siebenmorgen, R. and Krügel, E., 2010, *A&A*, 511, A6
- Smith, J. D. T., Draine, B. T., Dale, D. A., Moustakas, J., Kennicutt, Jr., R. C., Helou, G., Armus, L., Roussel, H., Sheth, K., Bendo, G. J., Buckalew, B. A., Calzetti, D., Engelbracht, C. W., Gordon, K. D., Hollenbach, D. J., Li, A., Malhotra, S., Murphy, E. J. & Walter, F. 2006, *ApJ*, 656, 770
- Smith, J. D. T., Armus, L., Dale, D. A., Roussel, H., Sheth, K., Buckalew, B. A., Jarrett, T. H., Helou, G., & Kennicutt, Jr., R. C. 2007, *PASP*, 119, 1133
- Sofia, U. J. 2004, *Astronomical Society of the Pacific Conference Series*, 309, 393
- Steiman-Cameron, T. Y., Haas, M. R., Tielens, A. G. G. M. and Burton, M. G., 1997, *ApJ*, 478, 261
- Sternberg, A. and Neufeld, D. A. 1999, *ApJ*, 516, 371
- Takami, M., Usuda, T., Sugai, H., Kawabata, H., Suto, H. and Tanaka, M., 2000, *ApJ*, 529, 268
- Tielens, A. G. G. M., Meixner, M. M., van der Werf, P. P., Bregman, J., Tauber, J. A., Stutzki, J. and Rank, D., 1993, *Science*, 262, 86
- Tielens, A. G. G. M., "The Physics and Chemistry of the Interstellar Medium", 2005
- Tielens, A. G. G. M., 2005, *ARA&A*, 46, 289
- van Dienenhoven, B. and Peeters, E. and Van Kerckhoven, C. and Hony, S. and Hudgins, D. M. and Allamandola, L. J. and Tielens, A. G. G. M., 2004, *ApJ*, 611, 928
- Witt, A. N., Stecher, T. P., Boroson, T. A. and Bohlin, R. C., 1989, *ApJ*, 336, 21



Table 1. Literature Properties of Sample PDRs

	NGC 7023	NGC 2023N (pos.1)	NGC 2023S (pos.2)	IC 63
Central Star	HD 200775	HD 37903	HD 37903	$\gamma$ -Cas
Spectral Type	B2.5 Ve <sup>a</sup>	B1.5 V <sup>b</sup>	B1.5 V <sup>b</sup>	B0.5 IVe <sup>c</sup>
$T_{eff}$ (K)	17000 <sup>a</sup>	22000 <sup>b</sup>	22000 <sup>b</sup>	25000 <sup>c</sup>
$T_{gas}$ (K)	400-800 <sup>d</sup>	550	550	620 <sup>c</sup>
$n_H$ (cm <sup>-3</sup> )	10 <sup>3</sup> -10 <sup>6</sup> <sup>d</sup>	10 <sup>4</sup> -10 <sup>6</sup> <sup>e</sup>	10 <sup>3</sup> -10 <sup>6</sup> <sup>e</sup>	10 <sup>4</sup> -10 <sup>5</sup> <sup>c</sup>
$G_o$	2400 <sup>d</sup>	2200 <sup>e</sup>	3-4000 <sup>e</sup>	650 <sup>c</sup>

<sup>a</sup>Rogers et al. (1995)

<sup>b</sup>de Boer (1983)

<sup>c</sup>Jansen et al. (1994); Karr et al. (2005)

<sup>d</sup>Fuente et al. (2000); Lemaire et al. (1996); Chokshi et al. (1988)

<sup>e</sup>Draine & Bertoldi (1996); Steiman-Cameron et al. (1997)

Table 2. Summary of *Spitzer* Observations

Object	Obs. Date	Program ID	Target RA	Target DEC	Exposure Time (s)	Number of exposures	Background Type	Background ID
NGC 7023	Aug. 8, 2004	28	21:01:31	+68:10:43	14.68	30	Nearby Obs.	22
NGC 2023N	Mar. 12, 2005	3512	05:41:35	-02:12:41	14.68	21	Nearby Obs.	172
NGC 2023S	Oct. 8, 2007	30295	05:41:37	-02:16:45	29.36	108	SKY	–
IC 63	Jan. 7, 2005	3512	00:59:00	+60:53:10	14.68	31	Outrigger	–

Table 3. Average Properties for Regions with Calculated  $T_{gas}$

Object	Distance from Star (") <sup>a</sup>	$T_{avg}$ (K)	$N(H_2)_{avg}$ ( $10^{20} \text{ cm}^{-2}$ )	Avg. $I_{7.7}/I_{11.3}$	Avg. $G_o/n_H$	Ortho-para Ratio
NGC 7023	$41.9 \pm 11.7$	$873 \pm 273$	$0.54 \pm 0.53$	$6.06 \pm 1.74$	$0.39 \pm 0.38$	$1.96 \pm 0.67$
NGC 2023N	$174.8 \pm 14.4$	$522 \pm 35$	$0.94 \pm 0.33$	$5.53 \pm 0.84$	$0.32 \pm 0.12$	$1.64 \pm 0.54$
NGC 2023S	$67.0 \pm 24.0$	$689 \pm 149$	$0.58 \pm 0.40$	$5.38 \pm 1.00$	$0.27 \pm 0.10$	$1.26 \pm 0.57$
IC 63	$1192 \pm 8.5$	$637 \pm 51$	$0.26 \pm 0.10$	$3.23 \pm 0.38$	$0.10 \pm 0.02$	$1.99 \pm 0.37$

Note. —  $\pm$  values represent standard deviations of the values calculated, not the error

<sup>a</sup>Projected distance

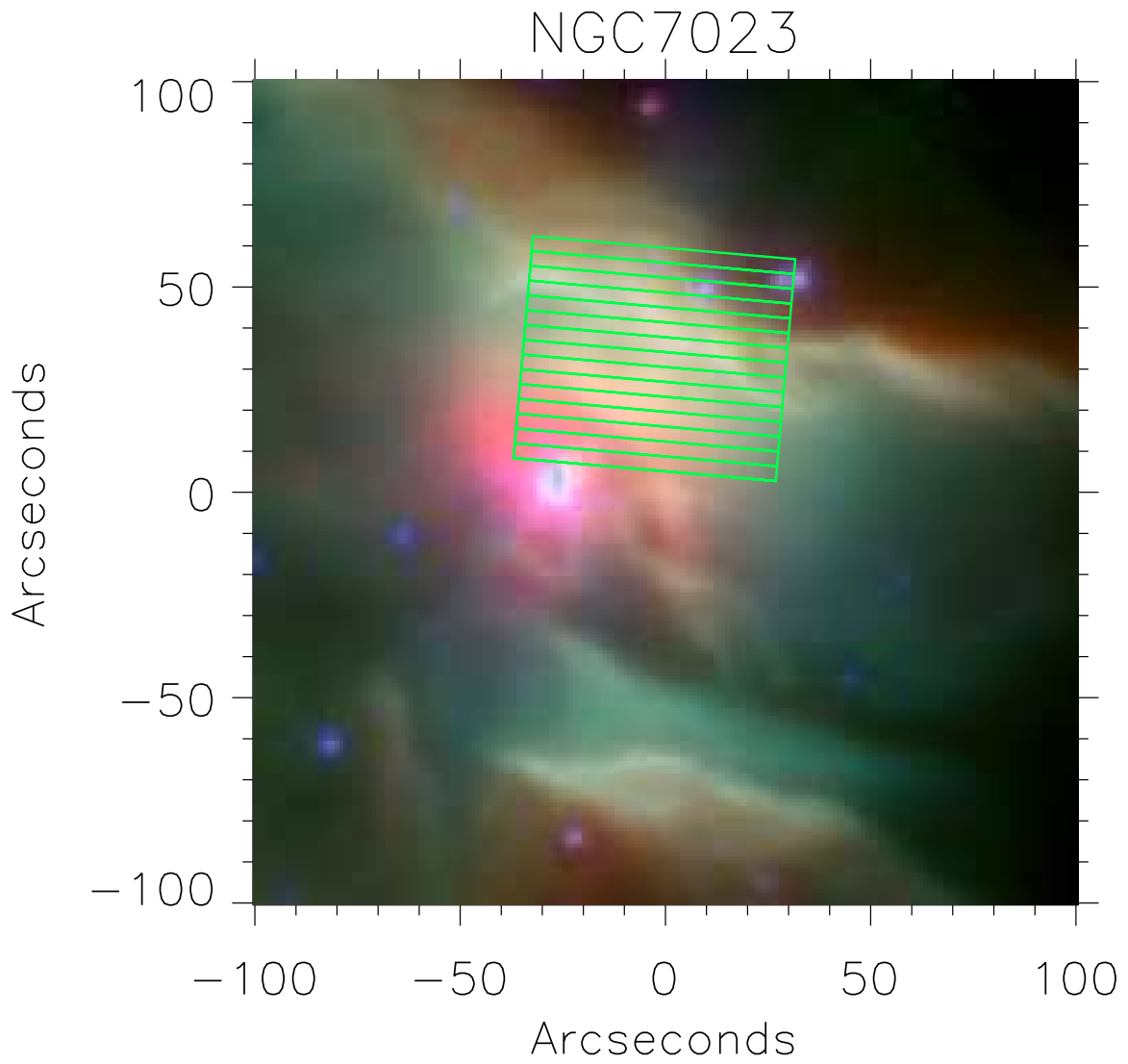


Fig. 1.— IRAC 3.6 $\mu\text{m}$ , 8 $\mu\text{m}$ , and MIPS 24 $\mu\text{m}$  image of NGC7023 with IRS slit overlays. Overlapping slits are merged. North is oriented up in this image.

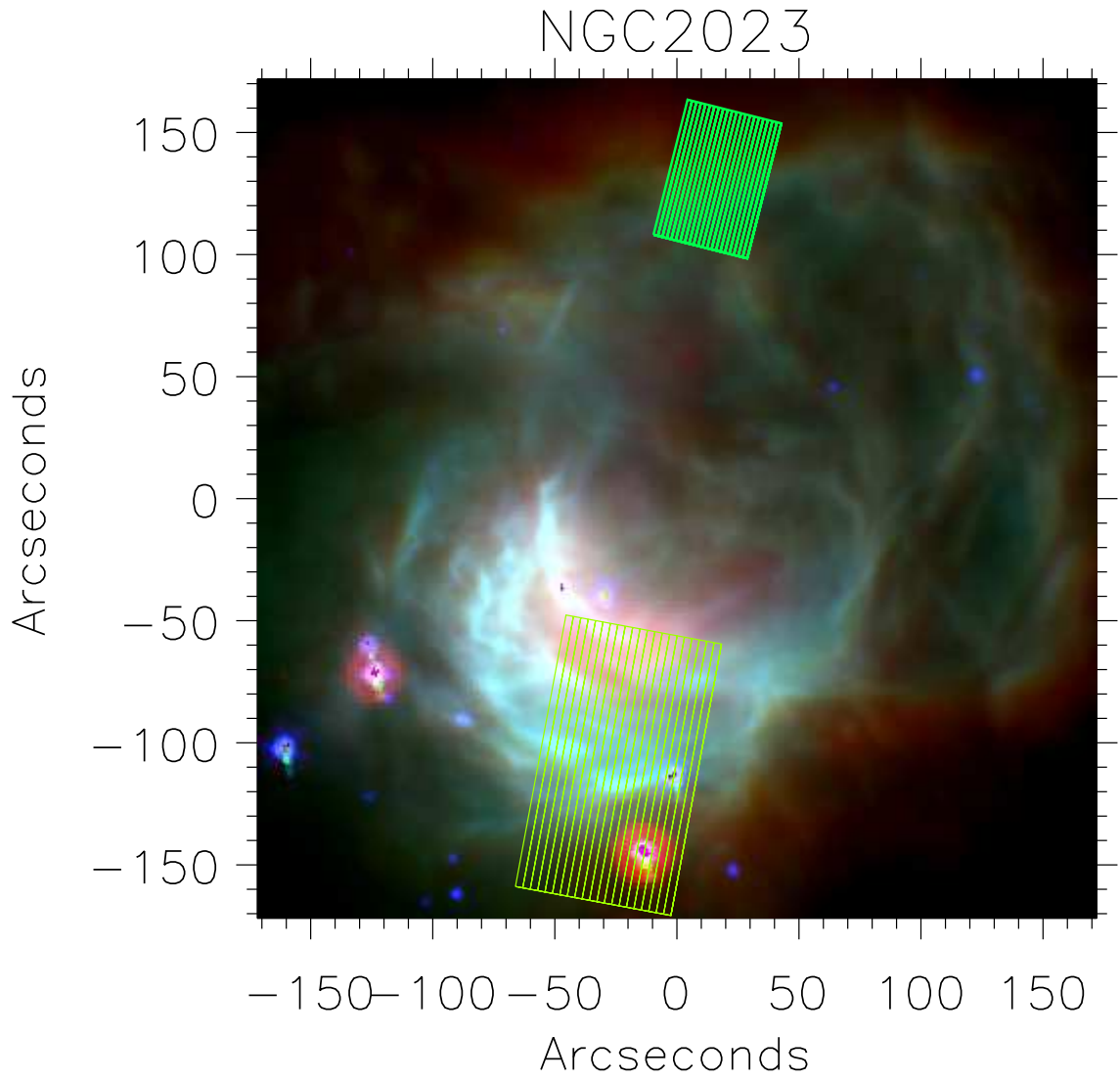


Fig. 2.— IRAC  $3.6\mu\text{m}$ ,  $8\mu\text{m}$ , and MIPS  $24\mu\text{m}$  image of NGC2023 with IRS slit overlays. Overlapping slits are merged. North is oriented up in this image.

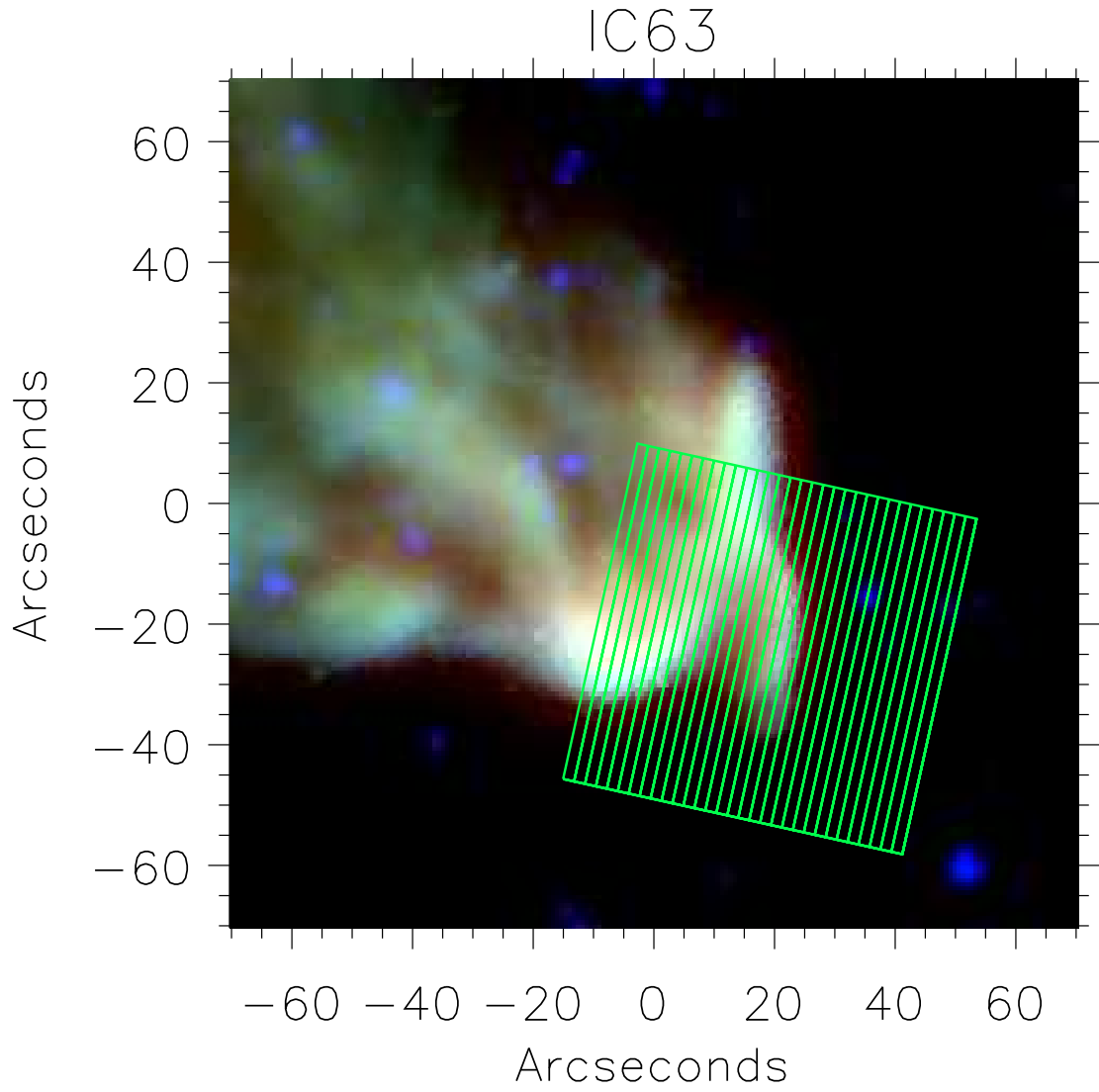


Fig. 3.— IRAC  $3.6\mu\text{m}$ ,  $8\mu\text{m}$ , and MIPS  $24\mu\text{m}$  image of IC63 with IRS slit overlays. The star  $\gamma$  Cas is approximately 1.3 pc SW of this emission nebula and not in this image. North is oriented up.



NGC 7023

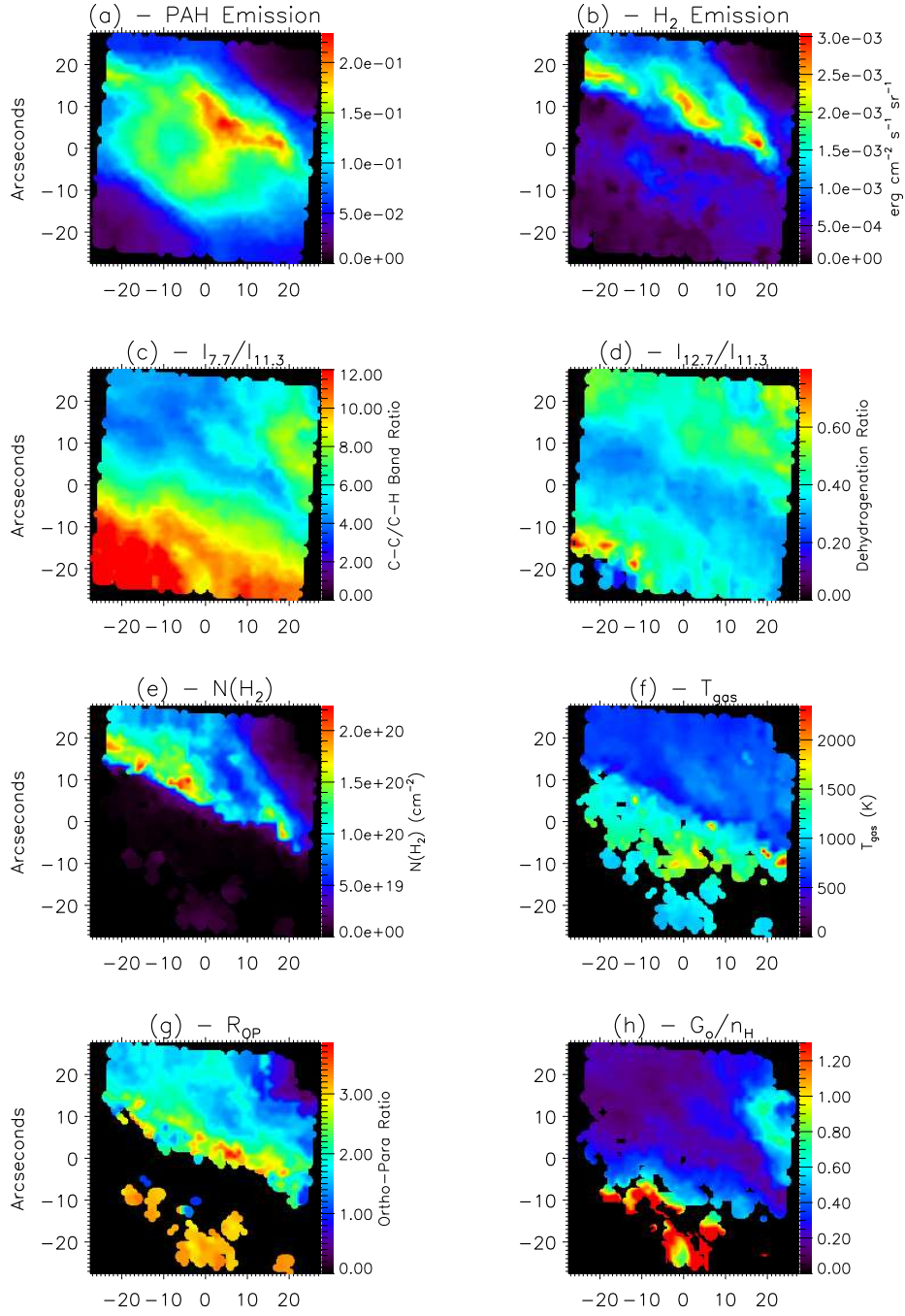


Fig. 4.— PAH and H<sub>2</sub> emission and diagnostics for NGC 7023. (a) Total detected PAH emission. (b) Total detected H<sub>2</sub> emission. (c)  $I_{7.7}/I_{11.3}$ . (d)  $I_{12.7}/I_{11.3}$ . (e) H<sub>2</sub> column density. (f) H<sub>2</sub> derived gas temperature. (g) H<sub>2</sub> Ortho-to-para ratio. (h)  $G_o/n_H$ .

NGC 2023<sup>42</sup> North

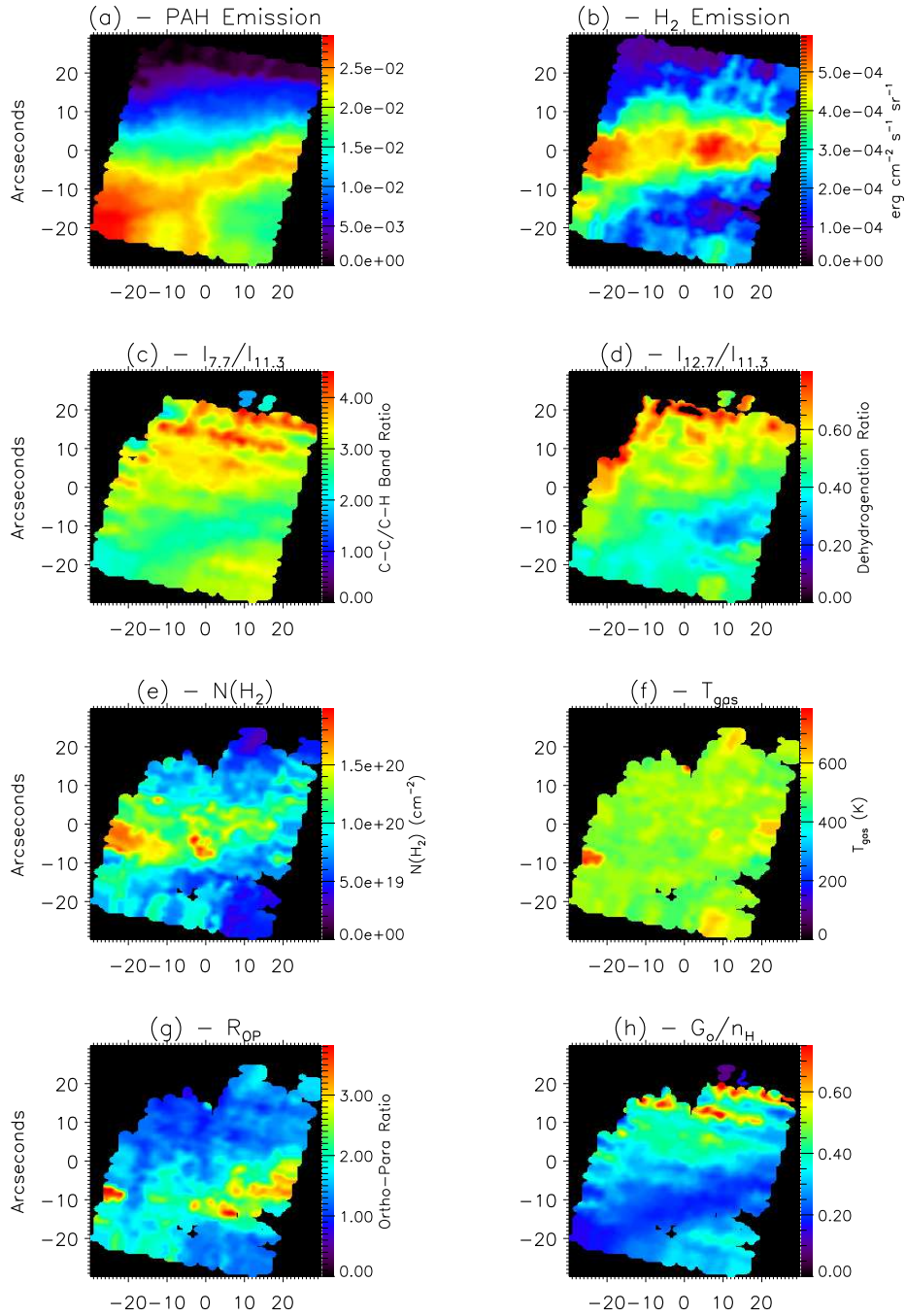


Fig. 5.— PAH and H<sub>2</sub> emission and diagnostics for NGC 2023 North. (a) Total detected PAH emission. (b) Total detected H<sub>2</sub> emission. (c)  $I_{7.7}/I_{11.3}$ . (d)  $I_{12.7}/I_{11.3}$ . (e) H<sub>2</sub> column density. (f) H<sub>2</sub> derived gas temperature. (g) H<sub>2</sub> Ortho-to-para ratio. (h)  $G_o/n_H$ .

NGC 2023<sup>43</sup> South

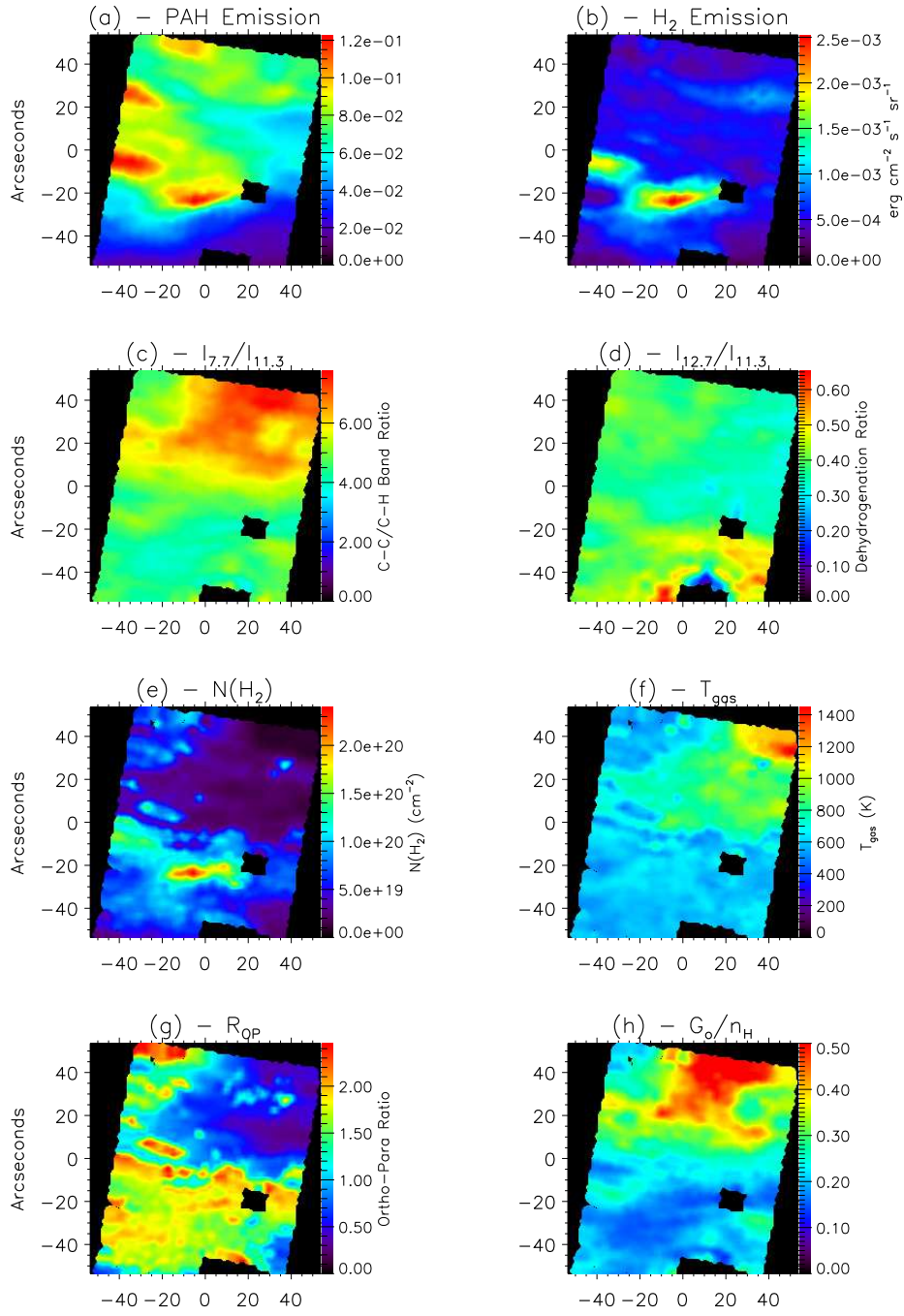


Fig. 6.— PAH and H<sub>2</sub> emission and diagnostics for NGC 2023 South. (a) Total detected PAH emission. (b) Total detected H<sub>2</sub> emission. (c)  $I_{7.7}/I_{11.3}$ . (d)  $I_{12.7}/I_{11.3}$ . (e) H<sub>2</sub> column density. (f) H<sub>2</sub> derived gas temperature. (g) H<sub>2</sub> Ortho-to-para ratio. (h)  $G_o/n_H$ .

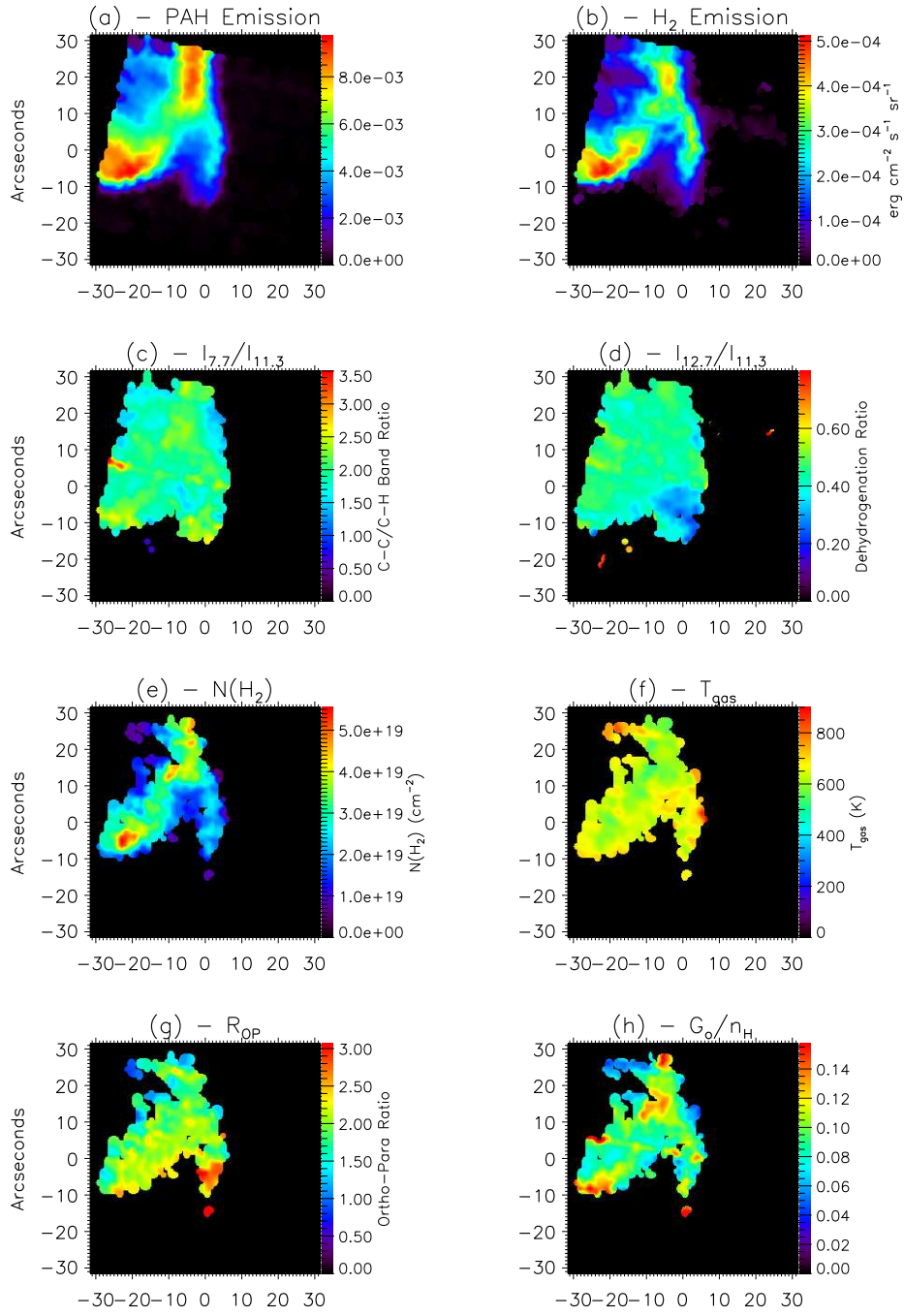


Fig. 7.— PAH and H<sub>2</sub> emission and diagnostics for IC 63. (a) Total detected PAH emission. (b) Total detected H<sub>2</sub> emission. (c)  $I_{7.7}/I_{11.3}$ . (d)  $I_{12.7}/I_{11.3}$ . (e) H<sub>2</sub> column density. (f) H<sub>2</sub> derived gas temperature. (g) H<sub>2</sub> Ortho-to-para ratio. (h)  $G_o/n_H$ .

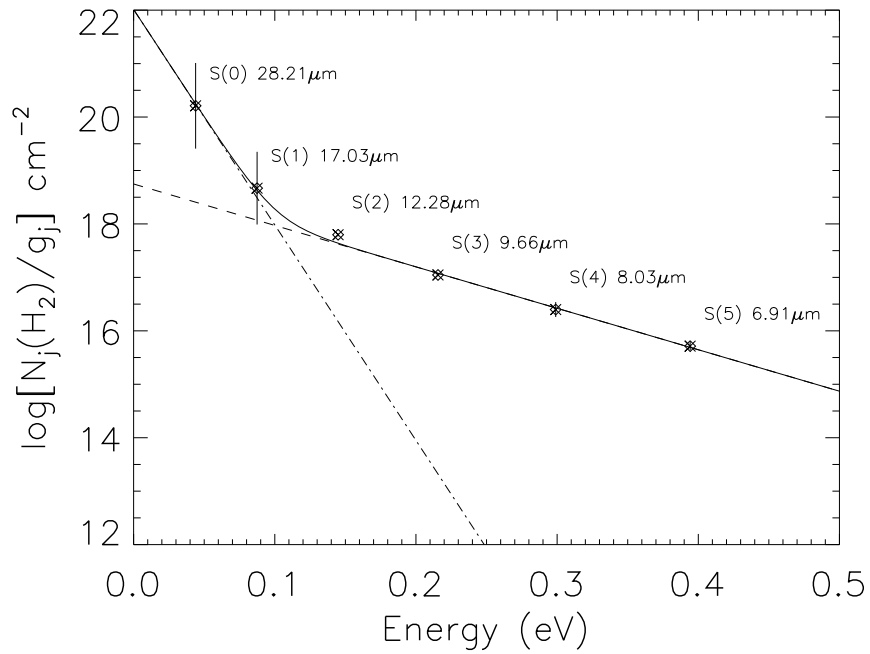


Fig. 8.— Plot of the  $\text{H}_2$  S(0) - S(5) rotational lines as a function of transition energy for a single data cube element near the bright ribbon of NGC 7023. Overplotted are two temperature fits, one for a higher column density gas ( $3.5 \times 10^{22} \text{ cm}^{-2}$ ) at 125K (dot-dash) and another for a lower column density gas ( $9 \times 10^{19} \text{ cm}^{-2}$ ) at 650K (dash).

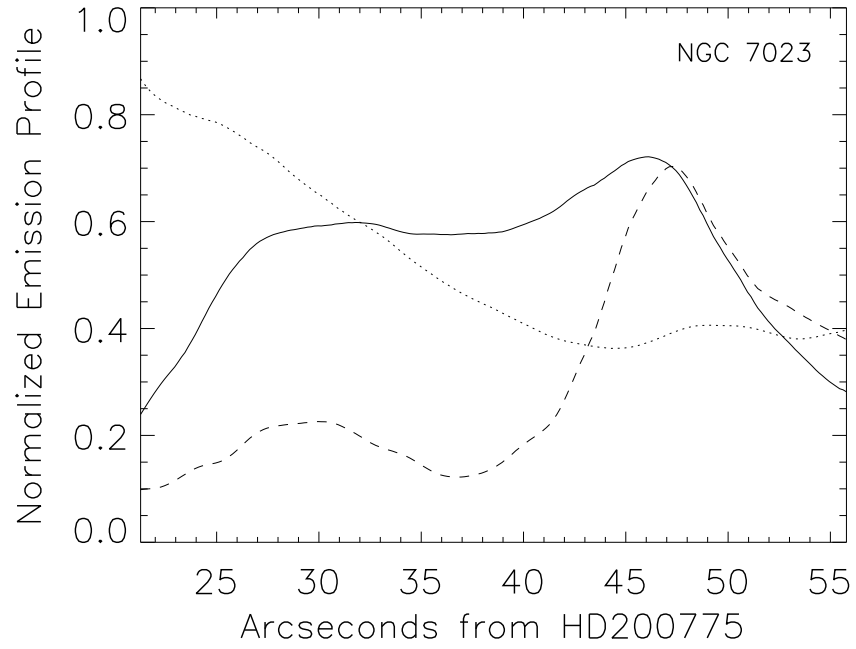


Fig. 9.— Average normalized emission profile for PAHs (solid), H<sub>2</sub> (dash) and  $(I_{7.7}/I_{11.3})/12$  (dot) for NGC 7023. Multiple cross-sections through the PDR originating from the direction of HD 200775 are averaged to produce this profile.

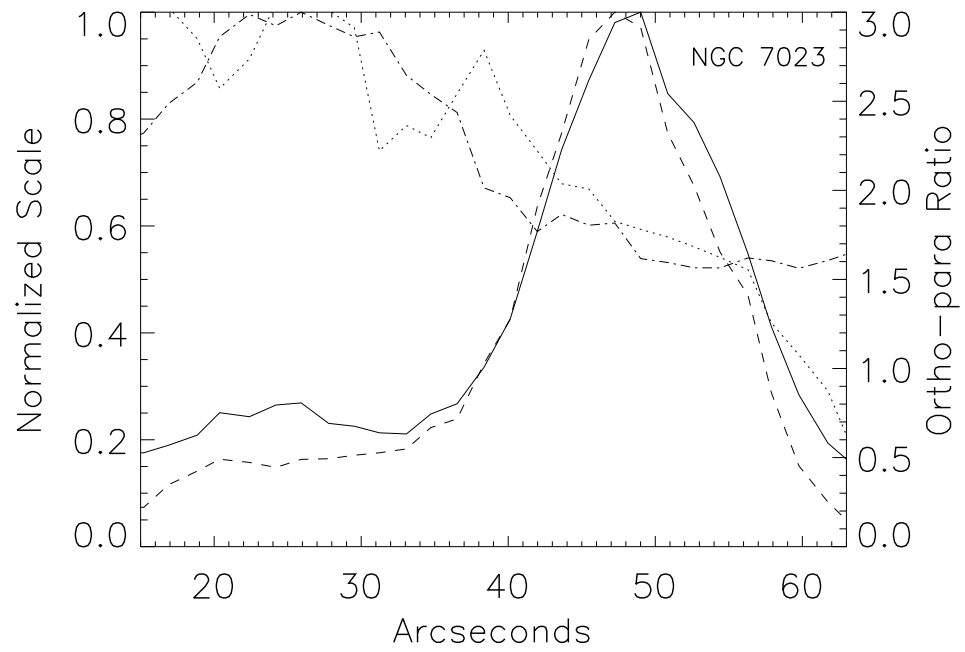


Fig. 10.— Plot of the ortho-H<sub>2</sub> S(3) (dash) and para-H<sub>2</sub> S(2) (solid) emission in NGC 7023 as a function of projected distance from the central star. Also plotted is the average normalized temperature profile (dash-dot) and the ortho-para ratio (dot).

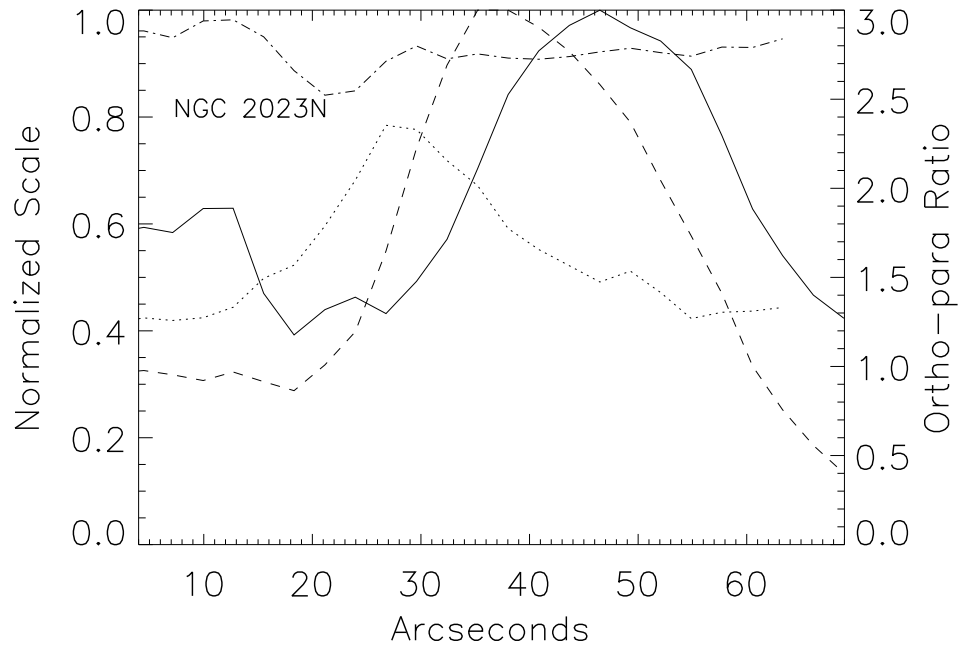


Fig. 11.— Plot of the total ortho-H<sub>2</sub> (dash) and para-H<sub>2</sub> (solid) emission in NGC 2023N as a function of projected distance from the lower right corner of the maps in Figure 5. Also plotted is the average normalized temperature profile (dash-dot) and the ortho-para ratio (dot).



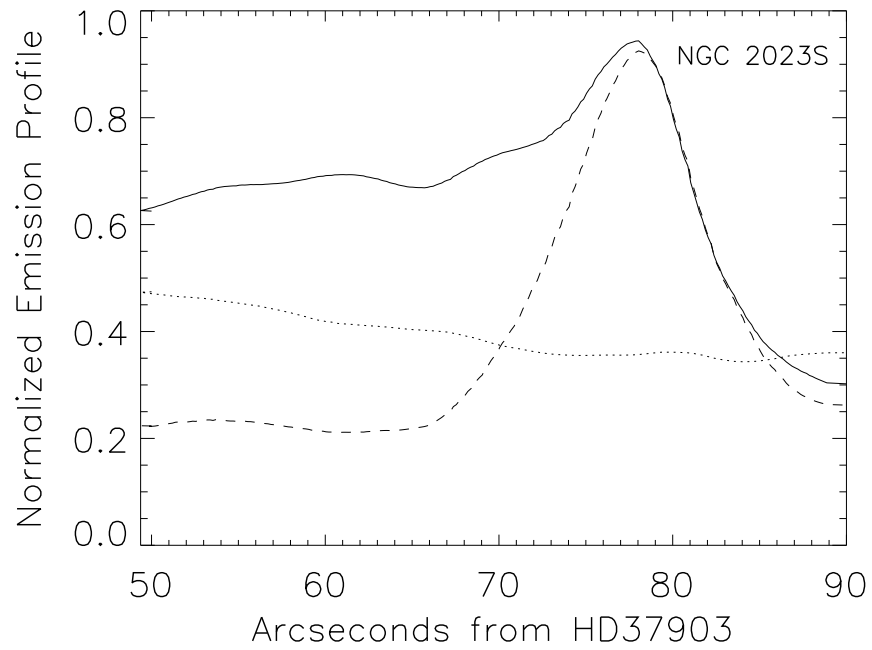


Fig. 12.— Average normalized emission profile for PAHs (solid), H<sub>2</sub> (dash) and  $(I_{7.7}/I_{11.3})/12$  (dot) for NGC 2023S. Multiple cross-sections through the PDR originating from the direction of HD 37903 are averaged to produce this profile.

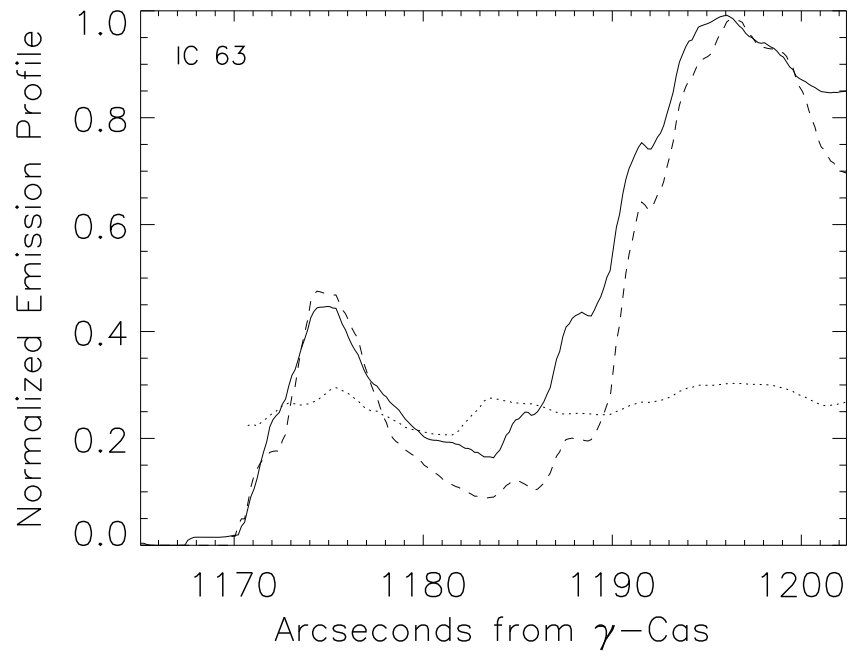


Fig. 13.— Average normalized emission profile for PAHs (solid), H<sub>2</sub> (dash) and (I<sub>7.7</sub>/I<sub>11.3</sub>)/12 (dot) for IC 63. Multiple cross-sections through the PDR originating from the direction of  $\gamma$ -Cas are averaged to produce this profile.

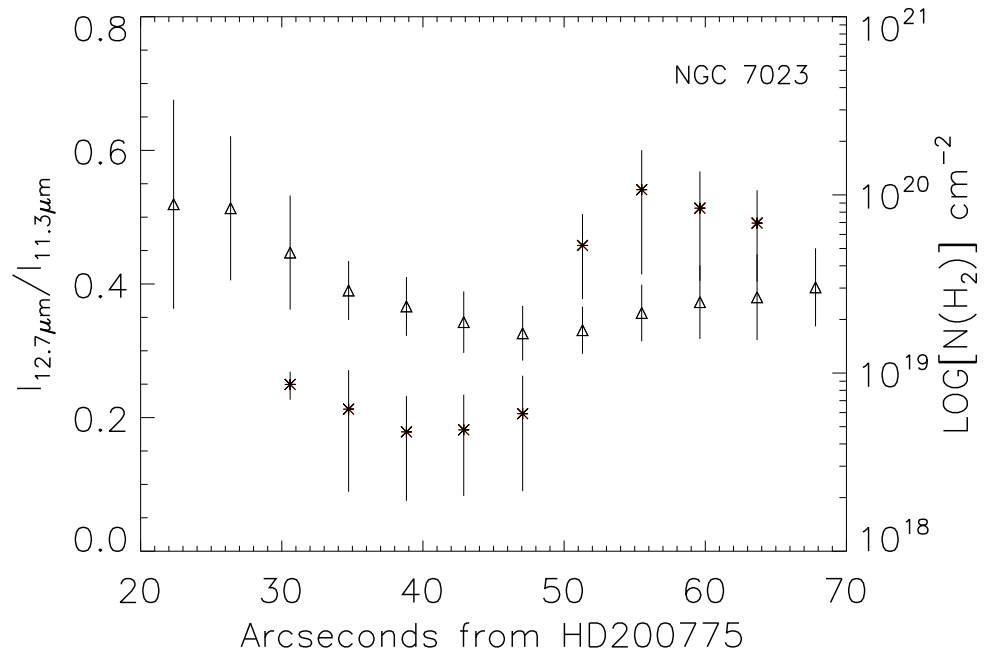


Fig. 14.— Plot of the average profiles of  $I_{12.7}/I_{11.3}$  (triangle) and  $N(\text{H}_2)$  (asterix) versus distance to HD 200775 in NGC 7023.